universität wien

MASTERARBEIT | MASTER'S THESIS

Titel | Title

Global Emissions of Hexafluoroethane Determined by Inverse Modeling

verfasst von | submitted by

Benjamin Erik Püschel BSc

angestrebter akademischer Grad | in partial fulfilment of the requirements for the degree of

Master of Science (MSc)

Wien | Vienna, 2025

Studienkennzahl lt. Studienblatt | Degree programme code as it appears on the student record sheet:	UA 066 614
Studienrichtung lt. Studienblatt | Degree programme as it appears on the student record sheet:	Masterstudium Meteorology and Climate Science
Betreut von | Supervisor:	Univ.-Prof. Mag. Dr. Andreas Stohl

Abstract

Hexafluoroethane (C_2F_6) is one of the most potent greenhouse gases with an atmospheric lifetime of approximately 10,000 years. It is primarily emitted during aluminium smelting and semiconductor manufacturing. While industries claim to have decreased emissions and bottom-up (BU) emission inventories show relatively low emissions, top down (TD) estimates based on atmospheric C_2F_6 concentration measurements suggest otherwise. This study employs a measurement-based inverse modelling method using the atmospheric transport model FLEXPART and the Bayesian inversion framework FLEXINVERT+ to quantify global and regional C_2F_6 emissions. The approach combines 100 d backward trajectories, initiated at each measurement, with a custom global reanalysis of C_2F_6 mixing ratios, allowing for optimisation of emissions in the timespan between 2004 and 2023. A newly proposed method, constraining inversion results to well-known global emission magnitudes (e.g. from simpler box models), significantly reduces unrealistic year-to-year variability of emissions and introduces an additional constraint in regions or periods with lower observational coverage. Results are generally in good agreement with previous regional and global TD studies, but consistently result in higher emissions than BU methods, particularly in more recent years. Global emissions estimated by the inversion on average amount to 2.17 ± 0.25 kt/yr in 2007-2011, decreased to 1.81 ± 0.10 kt/yr for 2012-2016 and recently increased again to 2.18 ± 0.11 kt/yr in 2017-2021. The study finds that China contributes the largest share of global emissions at 55.8 ± 3.7 % in recent years and exhibits the highest absolute emission growth. Additionally, results indicate that emissions from India are of increasing importance due to its emerging aluminium industry, but are highly uncertain due to low observational coverage and large differences in BU datasets. C_2F_6 emission reductions in the US, EU, Japan, and other economically developed regions had offset increasing emissions in China and India during the 2000s and early 2010s, but have failed to do so in recent years leading to the increase of global emissions. These findings highlight the need for improved emission reporting and industry data availability to decrease the global TD-BU discrepancy. Expanding the global C_2F_6 measurement network, particularly in India, the Middle East, South America and Africa could significantly increase the robustness of global inverse modelling results and help constrain future emissions in regions where emissions are expected to increase most.

Zusammenfassung

Hexafluorethan (C_2F_6) ist eines der stärksten Treibhausgase mit einer atmosphärischen Lebensdauer von etwa 10.000 Jahren, das hauptsächlich bei der Aluminiumschmelze und der Halbleiterherstellung emittiert wird. Während die Industrie selbst, anhand von Bottom-up (BU) Methoden, die auf Produktionsdaten und Berichten beruhen, davon ausgeht, ihre Emissionen verringert zu haben, ergeben sich bei der Verwendung von Messdaten gestützten Top-down Methoden (TD) große Diskrepanzen zwischen den Ergebnissen beider Ansätze. In dieser Studie wird die auf Messungen basierte inverse Modellierung, unter Verwendung des atmosphärischen Transportmodells FLEXPART und des Bayes'schen Inversionsmodells FLEXINVERT+, angewandt, um globale und regionale C_2F_6 Emissionen zu ermitteln. Der Ansatz kombiniert Rückwärts-Trajektorien über 100 Tage, initialisiert bei jeder Messung, mit einer eigens erstellten globalen Reanalyse von C_2F_6 Mischungsverhältnissen, was eine Ermittelung der Emissionen zwischen 2004 und 2023 ermöglicht. Eine neu entwickelte Methode, bei der die Inversionsergebnisse auf bereits etablierte globale Emissionswerte (z. B. aus einfacheren Box-Modellen) beschränkt werden, reduziert unrealistische Variabilität der Emissionen und führt eine zusätzliche Beschränkung in Regionen oder Zeiträumen mit geringerer Beobachtungsabdeckung ein. Die Ergebnisse weisen insgesamt eine gute Übereinstimmung mit regionalen und globalen TD-Studien auf, liefern aber höhere Emissionen als die mit BU-Methoden ermittelten, insbesondere in den letzten Jahren. Die von der Inversion errechneten globalen Emissionen belaufen sich im Durchschnitt auf $2,17 \pm 0,25\,\mathrm{kt/Jahr}$ im Zeitraum 2007-2011, gingen während 2012-2016 auf $1,81 \pm 0,10\,\mathrm{kt/Jahr}$ zurück und stiegen wieder auf $2,18 \pm 0,11\,\mathrm{kt/Jahr}$ im Zeitraum 2017-2021 an. Die Studie zeigt, dass China in den letzten Jahren mit $55,8 \pm 3,7\,\%$ den größten Anteil an den weltweiten Emissionen hatte und das höchste absolute Emissionswachstum aufwies. Darüber hinaus zeigen die Ergebnisse, dass Emissionen in Indien aufgrund der aufstrebenden Aluminiumindustrie von zunehmender Bedeutung sind, aber aufgrund der geringen Beobachtungsdichte und großer Unterschiede zwischen BU-Datensätzen mit großer Unsicherheit behaftet sind. Die Verringerung der C_2F_6-Emissionen in den USA, der EU, Japan und anderen wirtschaftlich entwickelten Regionen konnte den Anstieg der Emissionen in China und Indien in den 2000er und frühen 2010er Jahren ausgleichen, was jedoch in den letzten Jahren nicht gelungen ist und zu einem Anstieg der globalen Emissionen führte. Diese Ergebnisse unterstreichen die Notwendigkeit von verbesserten Methoden zur BU Emissionsermittlung und der Verfügbarkeit von Industriedaten, um die globale TD-BU-Diskrepanz zu verringern. Eine Ausweitung des globalen C_2F_6-Messnetzes, insbesondere in Indien, dem Nahen Osten, Südamerika und Afrika, könnte die Stabilität der Ergebnisse der inversen Modellierung deutlich erhöhen und dazu beitragen, Emissionen in den Regionen besser einzuschränken, in denen der größte Emissionsanstieg zu erwarten ist.

Acknowledgements

Acknowledgements are made to the AGAGE team for providing measurement data. AGAGE is supported principally by the National Aeronautics and Space Administration (USA) grants to the Massachusetts Institute of Technology and the Scripps Institution of Oceanography. AGAGE operations are supported by CSIRO and BoM (Australia), NRF (S. Korea), FOEN (Switzerland), DESNZ (Ireland), BMBF (Germany) and NILU (Norway). The team at CMA is acknowledged for performing measurements in China. People at NOAA are thanked for performing and publishing measurement data. I want to thank Lucie Bakels, Michael Blaschek, Marina Dütsch, Luise Kandler, Seyed Omid Nabavi, Rona Thompson, Petra Seibert and Christine Groot Zwaaftink for their support and interesting discussions, as well as Andreas Stohl and Martin Vojta for their continued support and supervision.

Table of Contents

List of Figures

1. Hexafluoroethane in the atmosphere

Hexafluoroethane (a.k.a. C_2F_6, PFC-116, perfluoroethane) is a non-flammable and odorless gas at room temperature and can be classified as a perfluorocarbon (PFC) or more broadly as a fully fluorinated compound. Other PFCs include tetrafluoromethane (CF_4) and octafluoropropane (C_3F_8), while sulfur hexafluoride (SF_6) or nitrogen trifluoride (NF_3) are examples of other fully fluorinated compounds.

Penkett et al. (1981) were the first to measure and publish an average background mixing ratios of C_2F_6 at 4.0 ± 0.9 pptv. They already suspected the gas to contribute to the greenhouse effect and their results indicated that pre-industrial mixing ratios were near 0 pptv suggesting no natural emissions. An exceptionally long atmospheric lifetime is also mentioned, adding to a list of attributes which would later be confirmed multiple times. Later measurements revealed that these first measurements were too high by a factor of 2 and reported Northern Hemisphere (NH) mid-latitude mixing ratios to be around 2 pptv in the troposphere during the early 1980s (Fabian et al., 1987). The measured negative vertical gradient suggested either high anthropogenic build-up in the troposphere or decomposition in the stratosphere and above, or both. A few years later, the Intergovernmental Panel on Climate Change (IPCC) first mentioned PFCs, including C_2F_6, acknowledging them as greenhouse gases GHG and initiating further research into these compounds (Change, 1992).

Ravishankara et al. (1993) then calculated an atmospheric lifetime of 10.000 y, a value still used today in the scientific community (IPCC, 2023). While UV photolysis and reaction with $O(^1D)$ and O^+ in the mesosphere and thermosphere (>60 km) could be identified as loss processes, they alone are too inefficient to achieve the lifetime of 10.000 y (Morris et al., 1995; Ravishankara et al., 1993). The main sink of C_2F_6 turns out to be thermal destruction in high temperature combustors, such as power plants, incinerators, and internal combustion engines or during natural events such as volcanic eruptions and lightning strikes. However, natural sinks are likely negligible as without anthropogenic sinks, the lifetime would increase to approximately 450.000 years (Ravishankara et al., 1993).

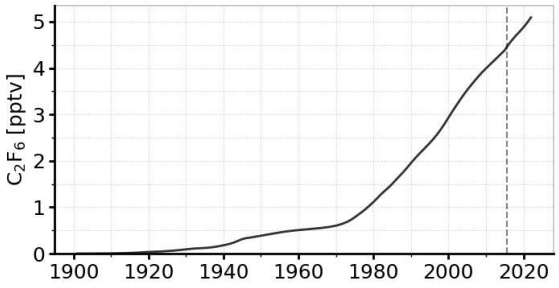

Fig. 1 Annual mean Southern Hemisphere (SH) C_2F_6 mixing ratios. Data from Trudinger et al. (2016) between 1900 and 2015, measurements at Cape Grim (Tasmania) between 2016 and 2023. Cape Grim predominantly receives "clean" air from the southern mid-latitudes, which is representative of the background conditions in its hemisphere.

Roehl et al. (1995) presented the first estimation of C_2F_6's global warming potential (GWP), a concept introduced to assess a GHG's effectiveness in causing radiative forcing compared

to CO_2 (IPCC, 2023). Their calculation resulted in a GWP of 20.870 over a time horizon of 100 yr, making C_2F_6 one of the most potent GHGs known to humans. In later studies, the GWP estimates over 100 yr were reduced to 13,200, a value still higher than for most other GHGs (Hodnebrog et al., 2020). Fortunately, atmospheric mixing ratios are very low compared to other GHGs (≈ 5 ppt in the early 2020s, see Fig. 1 for a mixing ratio time series), resulting in a low effective radiative forcing of 1.4 mW/m^2 (major GHGs for comparison: CO_2: 2156 mW/m^2, CH_4: 544 mW/m^2). C_2F_6's contribution to earth's current radiation imbalance is therefore negligible at less than 0.1%. However, when (or if) anthropogenic emissions of short-lived GHGs are reduced, their mixing ratios will drop over time while C_2F_6's mixing ratio will remain nearly constant leading to a higher contribution in total radiative forcing. This problem becomes apparent when comparing GWPs over different time horizons, revealing a value of 18.200 over a period of 500 yr, although even this time period is short compared to C_2F_6's lifetime. The importance of C_2F_6 for global warming is further enhanced by the increasing atmospheric burden of C_2F_6, resulting from ongoing anthropogenic emissions.

1.1. Emissions of C_2F_6

C_2F_6 has no natural sources, meaning its entire atmospheric abundance originates from human activities (Trudinger et al., 2016). Until now, two major and several minor sectors contributing to global emissions have been identified. The following sections detail processes and mechanisms responsible for releasing the GHG into the atmosphere:

Aluminium industry

In the aluminium industry, PFCs, including C_2F_6, are emitted during an irregular event in the electrochemical smelting process referred to as anode effects (AE), where an insufficient amount of alumina (aluminium oxide) is present in the reduction cell. This effect leads to elevated cell voltages triggering a reaction that produces several gases including CF_4 and C_2F_6 (Marks & Bayliss, 2011). Wong et al. (2015) also suspect PFC emissions during standard conditions and low-voltage AE which might occur more often than high-voltage ones. Furthermore, different types of cell technologies result in different amounts of C_2F_6 emissions per ton of produced aluminium (IAI, 2020). China is identified as the biggest aluminium producer at 60% of global production followed by India and Russia, both at $\approx 6\%$ respectively (IAI, 2021). Until 2019, the industry claims to have reduced its C_2F_6 emissions to 35% of the amount in 1990, while increasing primary aluminium production by a factor of 3 (IAI, 2020). Independent studies confirm the general reduction but estimate smaller decreases in emissions and also point out that all of the emission reduction was achieved between 1990 and 2000. Since 2000 emissions have stayed relatively constant or increased slightly, likely due to a rapid expansion of the Chinese aluminium industry (Kim et al., 2014, 2021). For C_2F_6 emissions, this seems to imply

that the mitigation technologies improve at a similar rate to the total growth in aluminium production. Globally, the aluminium industry is estimated to account for $\approx 50\%$ of all C_2F_6 emissions, although this value is highly uncertain (see sec. 2.1) (Kim et al., 2021).

Semiconductor industry

There are two main use cases of C_2F_6 during the manufacturing of semiconductors. First, it is used to dry clean the inside of the chambers in which thin layers of silicon are deposited, a process called chemical vapor deposition (CVD). Unwanted deposition on the chamber walls is cleaned with fluorine chemistry, for which C_2F_6 represents a safe source that does not contaminate the silicon wafers. Secondly, PFCs including C_2F_6 are used as etchants to remove silicon-based material and produce patterns of integrated circuits (Illuzzi & Thewissen, 2010). While for the application of CVD chamber cleaning C_2F_6 can be easily replaced by less harmful gases such as NF_3, its properties as an etchant cannot be reproduced by other fluorine containing gases. For both processes, the industry is trying to reduce emissions by abatement, i.e. destroying the compound after it has been used (Beu, 2005; Illuzzi & Thewissen, 2010). Global emissions peaked during the early 2000s, declined until the early 2010s, and started to rise again since then (Kim et al., 2014; WSC, 2011, 2021). The emission decline was achieved by substitution of C_2F_6 as a CVD chamber cleaning gas and successful abatement implementation. The later rise can likely be attributed to the strong growth of the semiconductor industry and possibly underperforming abatement techniques (Kim et al., 2014). Since the 1990s, the largest semiconductor industries are primarily located in East Asia, mainly Taiwan, China, South Korea, and Japan, while the USA's and Europe's industries also play a significant role (Ou et al., 2024). Globally, the semiconductor industry is estimated to account for $\approx 30\%$ of all C_2F_6 emissions (Kim et al., 2021). As for the aluminium industry, this value is highly uncertain and further discussed in sec. 2.1.

Miscellaneous sources

Several other C_2F_6 emitting sectors have been identified, but their contributions are estimated to be minor compared to the two previously mentioned sectors (Kim et al., 2021). The largest and most uncertain of these is the emission from rare earth metal smelting during AE conditions, similar to those occurring in aluminium smelters (Cai et al., 2018). Research on PFC emissions from the rare earth metal industry is sparse and estimates range from insignificant to larger than the aluminium industry's contribution (Vogel and Friedrich (2018), Kim et al. (2021), Calvo Buendia et al. (2019)). Similar to processes in the semiconductor industry, C_2F_6 is also emitted during the manufacture of flat panel displays and photo-voltaic cells (Calvo Buendia et al., 2019). Another application of the gas is as a part of the refrigerant blend R508, where releases into the atmosphere can occur due to leakages (Kim et al., 2014). Lastly, the production of C_2F_6 itself also leads to emissions, mainly due to leakages or controlled venting by the factories

(Calvo Buendia et al., 2019). Contributions from these miscellaneous sources fill the remaining gap of ≈ 20% of global C_2F_6 emissions according to Kim et al. (2021).

1.2. C_2F_6 regulations

The first attempt to regulate global C_2F_6 emissions was done by the United Nations Framework Convention on Climate Change (UNFCCC) under the Kyoto Protocol in 1997 (UNFCCC, 1997). It entered into force in 2005, setting emission targets for many industrialised countries (so-called Annex-I countries), which include most EU countries, USA, Russia, and Japan. Other large source regions such as China, India, Malaysia, or South Korea (so-called non-Annex-I countries) are not obliged by emission caps. Furthermore, the Kyoto Protocol requires all Annex-I countries to annually report estimates of their emissions of several GHGs, including C_2F_6 (UNFCCC, 1997). Non-Annex-I countries started biennial reporting of their emissions more recently in 2014 after a decision at the Conference of the Parties in 2011 (COP 17) (UNFCCC, 2012).

Additionally, industries themselves also express efforts to reduce their C_2F_6 emissions. Large parts of the aluminium industry, through efforts by the IAI, have committed to reduce their PFC emissions per ton of produced aluminium by 93% between 1990 and 2010 (Marks & Bayliss, 2011). According the the IAI's estimates the goal has nearly been achieved although absolute PFC emissions decreased only by 65% due to strong growth of the aluminium industry (high uncertainty for these estimations, see sec. 2.1) (IAI, 2020) (Kim et al., 2021). It has to be mentioned that the aluminium industry is economically motivated to reduce emissions, since avoiding PFC producing AE conditions results in increased aluminium production efficiency (Tabereaux & Peterson, 2014).

In 1999, the semiconductor industry also agreed to reduce their C_2F_6 emissions until 2010, which is claimed to have been achieved due to replacement by NF_3 for the application in CVD chamber cleaning (WSC, 2011). A new voluntary agreement for the period of 2011 to 2020 was then announced which aimed at reducing the normalised emission rate (amount of PFCs emitted per cm^2 of produced semiconductors), not absolute emissions due to the industry's strong growth (Czerniak, 2018; WSC, 2011). The normalised emission rate in 2020 was lower than 10 years prior but slightly above the expected value, while absolute emissions from the semiconductor industry increased during this period (Kim et al., 2021; WSC, 2021). In 2022 the World Semiconductor Council (WSC) announced its new goal to again reduce absolute emissions until 2030 (WSC, 2024). Some other, smaller contributing sectors have also set PFC emission reduction targets, such as the World LCD Industry Cooperation Committee (WLICC) for the LCD display industry (Nishida et al., 2005).

2. Bottom-up and top-down estimates of C_2F_6 emissions

Emission inventories can be categorised into two primary approaches: bottom-up (BU) and top-down (TD) methods. To construct a BU emission inventory of C_2F_6, industries' activity data (e.g. mass of produced primary aluminium) and their corresponding emission factors (e.g. mass of C_2F_6 emitted per mass of aluminium produced) are multiplied for each emitting sector. The IPCC provides guidelines outlining specific methods and emission factors to be selected based on the availability of data and the characteristics of the industry (Calvo Buendia et al., 2019). These approaches are adopted by countries to obtain the best estimate of their own total emissions which are then reported to the UNFCCC (UNFCCC, 2024a, 2024b). Additional industry data and UNFCCC reports are compiled in the Emissions Database for Global Atmospheric Research (EDGAR) to create a global emission inventory on a 0.1° x 0.1° grid (EDGAR, 2023; Olivier, 2022).

On the other hand TD methods utilise atmospheric measurements of a respective species to estimate its emission magnitude and distribution. While simple TD approaches such as interspecies correlation and back trajectory methods have been used successfully, the computationally more demanding method of inverse modelling has established itself due to superior accuracy (Fang et al., 2018; Flerlage et al., 2021). Global TD emission estimates of C_2F_6 have so far only been obtained with box models such as the AGAGE 12-box model, which does not allow for regional analysis of emissions (Mühle et al., 2010; Say et al., 2021; Trudinger et al., 2016). High-resolution models have been employed in regional studies on Europe and East Asia to also determine the spatial distribution of C_2F_6 emissions (An et al., 2024; Kim et al., 2021; Say et al., 2021). This work extends the application of high resolution models to the global scale for C_2F_6.

2.1. Opportunities and limitations of bottom-up inventories

When emissions are estimated using industry data, sector-specific emissions can be quantified to evaluate the contribution of each individual sector. The BU approach also enables the estimation of emissions at resolutions ranging from regional to factory levels, which is challenging to achieve using TD methods.

However, BU inventories are associated with significant uncertainties arising from a range of contributing factors. Data gaps in reports submitted to the UNFCCC arise from some countries either failing to report their emissions or providing aggregated values for all PFCs rather than reporting each compound individually. Data quality varies across countries and sectors due to differences in regulatory frameworks and the willingness of industries to disclose data (Kim et al., 2014). For instance, China, the world's largest aluminium-producing country, does not participate in a survey by the IAI, which collects data on AE conditions to improve global esti-

mates of PFC emissions from the aluminium industry. Another significant source of uncertainty arises from emission factors which relate industry activities to the release of C_2F_6 into the atmosphere. The cell technology employed in aluminium smelting can influence the emission factor by up to two orders of magnitude, introducing substantial errors when the specific technology is unknown. Even when the cell technology is identified, uncertainties exceeding 100% remain (IAI, 2020; Marks & Nunez, 2018). Similarly, emission factors of the semiconductor industry exhibit substantial variability depending on the specific manufacturing processes, wafer size, and type and implementation of abatement techniques, leading to significant uncertainties in emission estimates (Calvo Buendia et al., 2019). Contributions from other emitting sectors remain under-researched or may not even have been identified yet. The resulting uncertainties in total C_2F_6 emissions are significant, though they are often not explicitly quantified in BU inventories.

2.2. Inverse modelling: An independent emission estimation method

In general, an inverse problem refers to the mathematical concept of inferring the causes of a system's behaviour based on observations of its effects. Inverse modelling describes the computational approach used to perform this inference. When applied to estimating surface emissions of C_2F_6, atmospheric mixing ratio measurements ($\boldsymbol{y}$) from various monitoring stations are utilised to estimate the magnitude of emissions ($\boldsymbol{x}$) necessary to reproduce the observed mixing ratios. A linear forward operator ($\mathbf{H}$), containing information on atmospheric transport between source regions and measurement sites (receptors, hence the information the operator contains is often called the source receptor relationship (SRR)), defines the relationship between emissions and observations (e.g. Seibert and Frank (2004), Tarantola (2005), Thompson and Stohl (2014), Vojta et al. (2022)). Combining these components, we can formulate the forward model as follows:

$$\boldsymbol{y} = \mathbf{H}\boldsymbol{x}. \tag{1}$$

While prior information on emissions is generally required to solve this equation for regionally resolved emission estimates (see sec. 3.1), the method enables the estimation of emissions primarily based on atmospheric measurements, which are independent of the emissions themselves and their associated uncertainties. Thus, emissions estimated through inverse modelling can serve as an independent means to verify and identify potential gaps in bottom-up inventories. Air mass back-trajectory analysis can be used to identify measurements influenced by emission plumes from either the aluminium or semiconductor industry. This approach enables the determination of C_2F_6/CF_4 emission ratios, characteristic of the respective sector emissions. Kim et al. (2014) reported emission ratios of 0.10 ± 0.01 kg/kg for the aluminium industry and

$0.40 \pm 0.19\,\mathrm{kg/kg}$ for the semiconductor industry, values that are considered representative of these sectors globally. By applying this technique, industry contributions can be estimated from top-down emission data, provided that emissions of both CF_4 and C_2F_6 are well-known. It is important to note that this approach is not suitable when similar emission ratios are observed across multiple sectors, such as between the aluminium and rare earth metal industries or the semiconductor and flat-panel display industries. Nonetheless, since global C_2F_6 emissions predominantly originate from the aluminium and semiconductor industries, the approach can still provide valuable insights. However, obtaining detailed and reliable information on industry contributions comparable to BU data remains impossible using inverse modelling. Additional limitations of inverse modelling include challenges in representing uncertainties or limited observational constraints on emission regions, as discussed in sec. 6.

2.3. Discrepancies among C_2F_6 emission estimates

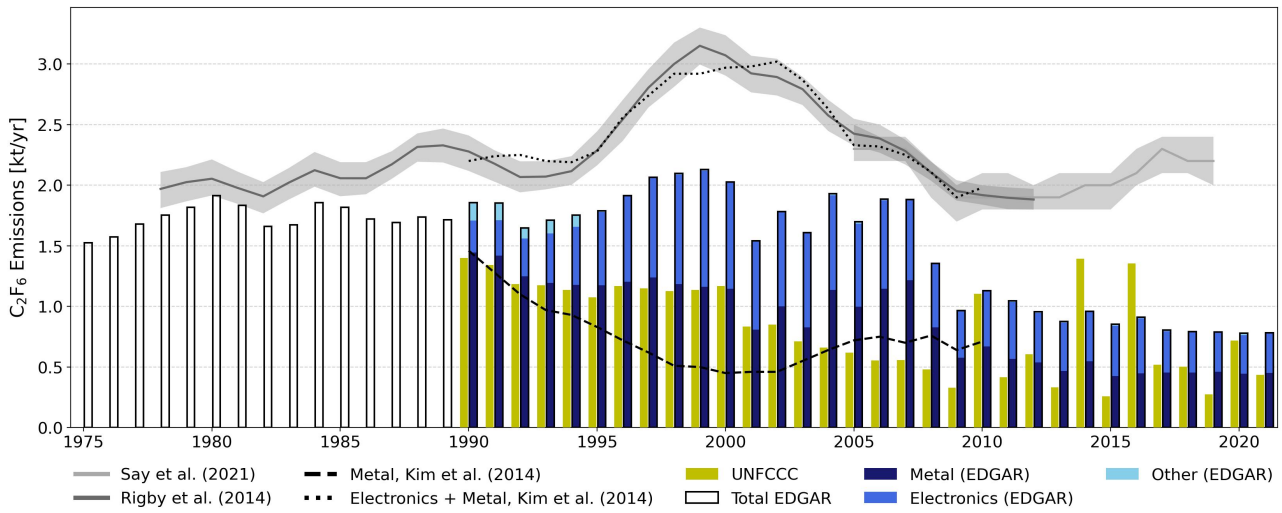

Fig. 2 Global TD (lines: Say et al. (2021), Rigby et al. (2014), Kim et al. (2014)) and BU (bars: EDGAR (2023), UNFCCC (2024a), UNFCCC (2024b)) C_2F_6 emission estimates. TD estimates diverge from BU inventories since the 1990s and particularly after 2007. EDGAR's sector contribution estimates from the metal and electronics industries and miscellaneous sources are shown in shades of blue after after 1990. Note that the high variability of UNFCCC estimates stem from gaps in submitted reports.

A comparison of global emissions compiled from several studies reveals a significant discrepancy between estimates derived from TD and BU methodologies since the 1990s (fig. 2). Until approximately 1995, both TD and BU estimates remain relatively constant at $\approx 2\,\mathrm{kt/yr}$. From 1995 to 2007, TD emissions increase to as much as $3\,\mathrm{kt/yr}$, while BU estimates remain relatively steady around $2\,\mathrm{kt/yr}$. After 2007, BU estimates decline to $\approx 1\,\mathrm{kt/yr}$, whereas TD emissions stabilize around $2\,\mathrm{kt/yr}$, with a slight upward trend observed over the past decade. Overall, TD

emissions are consistently higher than BU estimates throughout the entire four-decade period. In particular, UNFCCC reports account for only a fraction of the observed C_2F_6 increase in the atmosphere.

Using TD CF_4 emission estimates combined with specific C_2F_6/CF_4 emission ratios for the aluminium and semiconductor industries, Kim et al. (2014) apportioned total emissions between these two sectors. However, this method does not differentiate between emissions from the rare earth metal and aluminium industries or between the flat-panel display and semiconductor industries. As a result, sectors with similar emission ratios are grouped into broader categories, such as the metals and electronics industries. It is important to emphasize that the sector estimates are heavily influenced by uncertainties in both the TD emissions and the emission ratios.

The results indicate an overestimation of BU metal industry emissions during most of the study period (1990-2010), while emissions from the electronics industry seem to be the reason for the large discrepancy, especially since the early 1990s. Czerniak (2018) argue that the increasing complexity of semiconductor manufacturing has introduced additional steps where the release of C_2F_6 can occur. This complexity complicates accounting of emissions in BU inventories and likely leads to an overestimation of real-world abatement rates. Kim et al. (2014) also question the reliability of emission factors published by the IPCC (Calvo Buendia et al., 2019), noting that these factors are applied to a wide range of real-world manufacturing conditions, which they may not accurately represent.

In a regional BU study focused on China, Guo et al. (2023) achieved closer agreement with measurement-based TD estimates by utilizing PFC consumption data sourced from news reports, interviews with industry experts, and industry reports. Their analysis indicates that the primary discrepancy between their estimates, those of EDGAR, and China's official submission to the UNFCCC originates from the electronics sector, particularly the semiconductor industry. Specifically, Guo et al. (2023) estimate semiconductor industry emissions for 2021 at 450 t/yr, compared to electronics industry emissions of $<$50 t/yr reported by China and 54 t/yr estimated by EDGAR (EDGAR, 2023; Ministry of Ecology and Environment, 2024).

For the metal industry, primarily aluminium, it is generally assumed that BU estimates have lower uncertainty due to more extensive industry reporting and simpler emission estimation based on activity data compared to the electronics industry (IAI, 2020; Kim et al., 2021). Recent studies have demonstrated good agreement between BU and TD emission estimates for the metal industry in China, although EDGAR estimates are consistently lower (An et al., 2024; Kim et al., 2021). However, another regional study on Australian PFC emissions found that their BU inventory only accounted for 64% of emissions estimated with TD methods (Dunse et al., 2019). Wong et al. (2015) suspect non-detected AEs to be the main reason for the remaining discrepancy in the aluminium industry. No recent studies have presented global,

sector-specific TD emission estimates.

3. FLEXPART model family, data and methods for inverse modelling

To generate the TD emission estimate, the two distinct models FLEXPART and FLEXINVERT+ are employed. FLEXPART is used for two tasks: (1) simulating atmospheric transport between source regions and measurement sites (i.e. acquiring SRR) and (2) modelling mixing ratios prior to the backward simulation period (see secs. 3.3 and 3.4). The inversion (3) is performed using FLEXINVERT+ to estimate posterior emissions, combining prior knowledge with atmospheric measurements. FLEXPART is a Lagrangian Particle Dispersion Model (LPDM) calculating atmospheric transport, while FLEXINVERT+, a Bayesian inversion algorithm, estimates surface fluxes (Bakels et al., 2024; Thompson & Stohl, 2014)). Details about the models, their configurations, and the measurement data are provided in the following chapters. Data analysis, visualisation, and basic pre- and post-processing steps were conducted using Python in a Jupyter Notebook environment. Model simulations and more complex pre- and post-processing tasks were performed using existing Fortran code.

3.1. Theory of atmospheric inverse modelling

The forward model (eq. 1) computes theoretical atmospheric measurements $\boldsymbol{y}$ based on known atmospheric transport ($\mathbf{H}$) and emissions ($\boldsymbol{x}$). Hereafter, $\boldsymbol{x}$ will be referred to as the state vector, as it not only contains emissions, but also the baseline which will be explained in sec. 3.4. However, we are not interested in the forward but the inverse model, which aims to estimate the state vector given measurements and atmospheric transport information. This inverse problem is ill-conditioned or in some cases ill-posed, meaning small perturbations in the atmospheric model and measurements can induce significant variations in the estimated state or various emission patterns and magnitudes can reproduce the same measured mixing ratios (Kabanikhin, 2008). To solve the inverse problem (i.e. make it well-conditioned or well-posed if applicable), Bayes' theorem is applied to introduce a priori (prior) information on the state ($\boldsymbol{x}_p$) and additionally assign uncertainties to all model components. The prior state $\boldsymbol{x}_p$ serves as an independent initial estimate of the state vector, now termed the a posteriori (posterior) state $\boldsymbol{x}$. The optimal estimate of the posterior state is obtained by minimising the deviation between the prior and posterior state ($\boldsymbol{x} - \boldsymbol{x}_p$) while simultaneously minimising the difference between mixing ratio measurements and modelled posterior mixing ratios ($\boldsymbol{y} - \mathbf{H}\boldsymbol{x}$). Under the assumption of Gaussian distribution of all uncertainties, the following cost function is defined to achieve the optimal state estimate, when $J(\boldsymbol{x})$ is minimised (Tarantola, 2005; Thompson &

Stohl, 2014):

$$J(\boldsymbol{x}) = \frac{1}{2}(\boldsymbol{x} - \boldsymbol{x}_p)^T \mathbf{B}^{-1}(\boldsymbol{x} - \boldsymbol{x}_p) + \frac{1}{2}(\mathbf{H}\boldsymbol{x} - \boldsymbol{y})^T \mathbf{R}^{-1}(\mathbf{H}\boldsymbol{x} - \boldsymbol{y}), \tag{2}$$

where $\mathbf{B}$ represents the prior error covariance matrix and $\mathbf{R}$ is the observation error covariance matrix. These matrices determine the relative influence of measurements and the prior state on the posterior state. Specifically, higher uncertainty in the prior and lower measurement uncertainty increases the influence of measurements, and vice versa. Details on the construction of $\mathbf{B}$ and $\mathbf{R}$ are provided in sec. 3.6. Minimising the cost function (eq. 2) yields the following analytical solution for the posterior state:

$$\boldsymbol{x} = \boldsymbol{x}_p + \mathbf{K}(\boldsymbol{y} - \mathbf{H}\boldsymbol{x}_p), \tag{3}$$

while the posterior error covariance matrix $\mathbf{A}$ is expressed as:

$$\mathbf{A} = (\mathbf{I} - \mathbf{K}\mathbf{H})\mathbf{B}. \tag{4}$$

The gain matrix $\mathbf{K}$ quantifies the increment of the posterior from the prior state and simultaneously defines the magnitude and distribution of uncertainty reduction from the prior uncertainty achieved during the inversion. The gain matrix can be computed using two equivalent formulations, where one of them is computationally more efficient depending on the sizes of $\boldsymbol{x}_p$ and $\boldsymbol{y}$ (i.e. sizes of $\mathbf{B}$ and $\mathbf{R}$). When $dim(\boldsymbol{x}_p) > dim(\boldsymbol{y})$, the formulation $\mathbf{K} = \mathbf{B}\mathbf{H}^T(\mathbf{H}\mathbf{B}\mathbf{H}^T + \mathbf{R})^{-1}$ is preferred, whereas the alternative expression $\mathbf{K} = (\mathbf{B}^{-1} + \mathbf{H}^T\mathbf{R}^{-1}\mathbf{H})^{-1}\mathbf{H}^T\mathbf{R}^{-1}$ is advantageous when $dim(\boldsymbol{x}_p) < dim(\boldsymbol{y})$ (Tarantola, 2005).

3.2. Atmospheric measurements of C_2F_6

The inversion is constrained by in-situ atmospheric C_2F_6 mixing ratio measurements collected from 32 stations worldwide, sourced from various GHG observation networks. These measurements are provided by the Advanced Global Atmospheric Gases Experiment (AGAGE) network (Prinn et al., 2018), the National Oceanic and Atmospheric Administration, Earth System Research Laboratories, Global Monitoring Laboratory (NOAA-ESRL-GML) Long-term Observations of Greenhouse gases and Ozone-depleting Substances (LOGOS) division (Vimont et al., 2015), the Chinese Meteorological Administration (CMA) (An et al., 2024; Yao et al., 2012) and the Norwegian Institute for Air Research (NILU) (Platt et al., 2024). The dataset comprises both continuous online measurements and instantaneous flask sample measurements, differing in their temporal resolution. A detailed overview of continuous measurement sites is provided in tab. 1, while flask sampling stations are listed in tab. A1, together with acronyms, location information, measurement frequencies, and operational periods. Additionally, geographic locations of stations are illustrated in fig. 3.

ID	Station name	Organisation	Location	Altitude	Interval	Period
CGO	Cape Grim, Tasmania	AGAGE	40.7°S, 144.7°E	94	2h	04.2004-06.2023
CMN	Monte Cimone, Italy	AGAGE	44.2°N, 10.7°E	2165	2h	10.2022-06.2023
GSN	Gosan, South Korea	AGAGE	33.3°N, 126.2°E	72	2h	11.2007-12.2019
JFJ	Jungfraujoch, Switzerland	AGAGE	46.5°N, 8.0°E	3559	2h	04.2008-06.2023
MHD	Mace Head, Ireland	AGAGE	53.3°N, 9.9°W	8	2h	11.2003-06.2023
RPB	Ragged Point, Barbados	AGAGE	13.2°N, 59.4°W	30	2h	05.2005-06.2023
SDZ	Shangdianzi, China	CMA	40.7°N, 117.1°E	291	2h	01.2011-12.2021
SMO	Cape Matatula, American Samoa	AGAGE	14.2°S, 170.6°W	42	2h	12.2006-16.2023
TAC	Tacolneston, United Kingdom	AGAGE	52.5°N, 1.1°E	64	2h	12.2012-06.2023
THD	Trinidad Head, USA	AGAGE	41.1°N, 124.2°W	107	2h	03.2005-06.2023
TOB	Taunus, Germany	AGAGE	50.2°N, 8.4°E	825	2h	02.2023-06.2023
ZEP	Zeppelin, Norway	AGAGE	78.9°N, 11.9°E	475	2h	09.2010-06.2023

Tab. 1 Sites of continuous atmospheric measurements. Note: Altitude is given in m.a.s.l.

All AGAGE measurements were conducted using the automated Medusa Gas Chromatography-Mass Spectrometry (GC-MS) system, capable of sampling up to 12 times per day. Further detail about the Medusa GC-MS system can be found in Miller et al. (2008). The NOAA-ESRL-GML network collects flask samples at intervals ranging from days to months, which are later analysed in the laboratory using the Perseus 1 GC-MS system. Similarly, NILU operates a station in Antarctica, where one flask sample per week is collected and measured with the Medusa GC-MS system. The CMA network includes one continuous monitoring station in Shangdianzi (SDZ) and several flask sample stations, all employing the Medusa GC-MS system to measure mixing ratios. All observations were calibrated to the SIO-07 scale; therefore, no conversion of measurements is necessary.

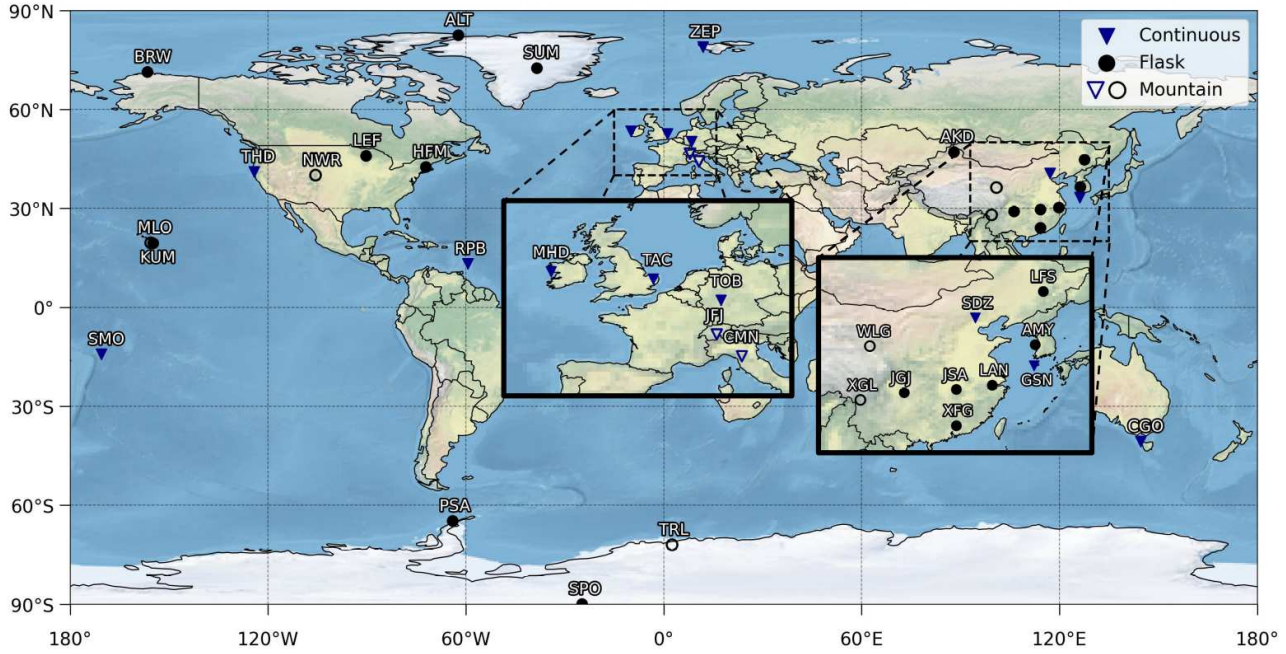

Fig. 3 Global distribution of atmospheric measurement sites. Continuous monitoring stations are marked with blue triangles, flask sampling sites with black circles, and mountain stations with the respective unfilled shape. The two black rectangles highlight regions with denser observational coverage in Europe and East Asia. No measurement stations are hidden underneath the two rectangles

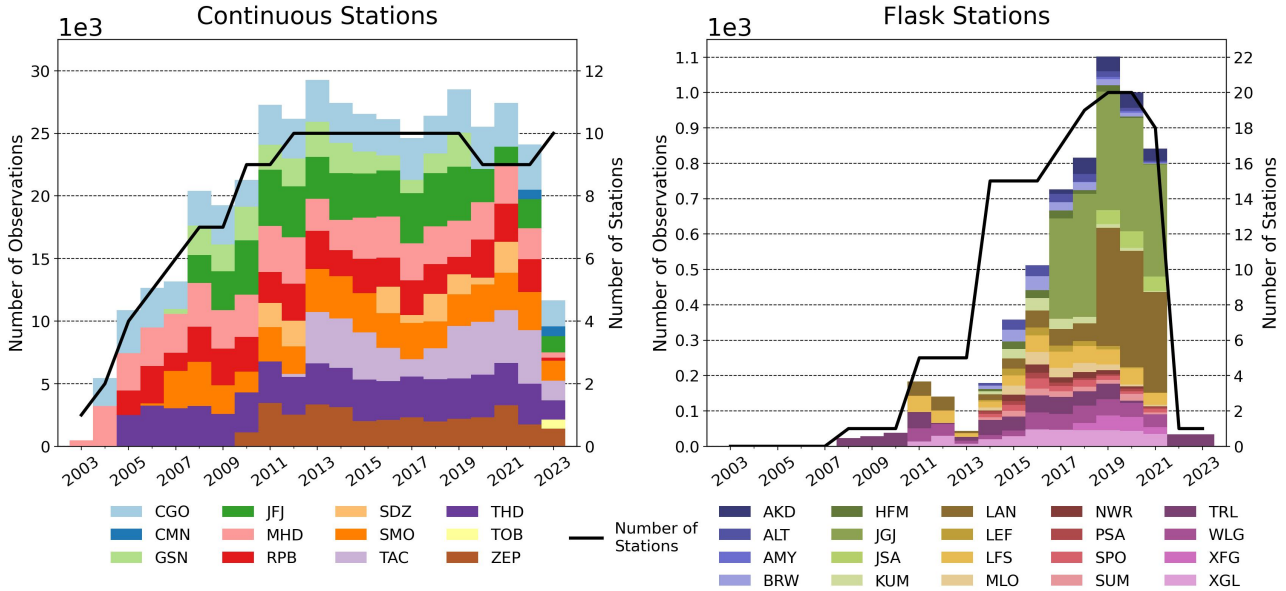

Fig. 4 Number of available individual observations (coloured bars, in thousands) and operational stations (black lines) as a function of time for continuous stations (left panel) and flask sampling stations (right panel).

Measurements began at Mace Head (MHD, Ireland) in late 2003. Until 2006, only 3 additional remote observation sites were operational. In subsequent years, continuous monitoring was

expanded to include sites closer to emission sources, such as Tacolneston (TAC, South East England), Jungfraujoch (JFJ, Switzerland) and key locations in East Asia, including Gosan (GSN, South Korea) and Shangdianzi (SDZ, North East China). Flask sampling by the CMA started in 2011, while NOAA-ESRL-GML began measuring samples in 2014. However, flask measurements accounted for only $0 - 3\%$ of total observations, depending on the year. Total measurement number and station coverage peaked in 2019 with nearly 30,000 individual air samples collected from 30 out of 32 operational stations. Limited data availability in 2022 and 2023 led to a significant reduction in observational coverage, particularly in East Asia, where no measurements have been reported since 2022. The inversion results presented in sec. 5 should be interpreted with consideration of this uneven observational coverage across regions. Additional details regarding annual measurement counts and station availability are shown in fig. 4. For the inversion, continuous measurements were averaged over 3 h intervals, while no temporal averaging was applied for their use in the global reanalysis simulation (sec. 3.4).

3.3. Source receptor relationship

The source receptor relationship (SRR) describes the atmospheric transport and is incorporated into the inversion as the transport matrix $\mathbf{H}_e$. This matrix relates C_2F_6 emissions $\boldsymbol{x}_e$ from a given grid cell at a given time to the resulting mixing ratio at measurement sites and their respective sample times. Therefore, it is sometimes referred to as emission sensitivity. $\mathbf{H}_e$ is expressed in units of residence time $\times$ volume per mass ($s\,m^3\,kg^{-1}$), resulting in the desired unit of mixing ratio at the measurement site when multiplied by an emission flux ($kg\,m^{-2}\,s^{-1}$) and integrated over the height of the lowest model layer.

To construct the SRR, the LPDM FLEXPART (version 10.4) (Pisso et al., 2019; Stohl et al., 1998) was run in a "backward in time" mode. This approach is computationally advantageous compared to the forward mode when the number of emission grid cells exceeds the number of measurement sites (Seibert & Frank, 2004). In each 3 h averaging interval around measurements, 50,000 virtual particles were released from the respective observation sites. Particles are then traced backward in time for 100 d using hourly wind fields from the ERA5 meteorological reanalysis dataset (Hersbach et al., 2020) by the European Centre for Medium-Range Weather Forecasts (ECMWF) at a 0.5° x 0.5° horizontal resolution and on 137 vertical levels.

The transport model can only account for emissions occurring within this 100 d backward simulation period at possible source locations reached by the virtual particles. Ideally, the backward simulation should span several centuries to include all historical emissions affecting present-day measurements. However, due to computational limitations, shorter periods of several days are typically simulated. Motivated by the findings of Vojta et al. (2022), who demonstrated that a longer simulation period of 50 d leads to more accurate and robust inversion results compared to shorter periods ($1 - 20$ d), a relatively long period was selected. The

extended simulation improves constraints on emissions from grid cells with large distances to observation stations by increasing the likelihood that particle trajectories reach these areas. Given the relatively sparse C_2F_6 measurement network, a particularly long backward simulation period of 100 d was feasible.

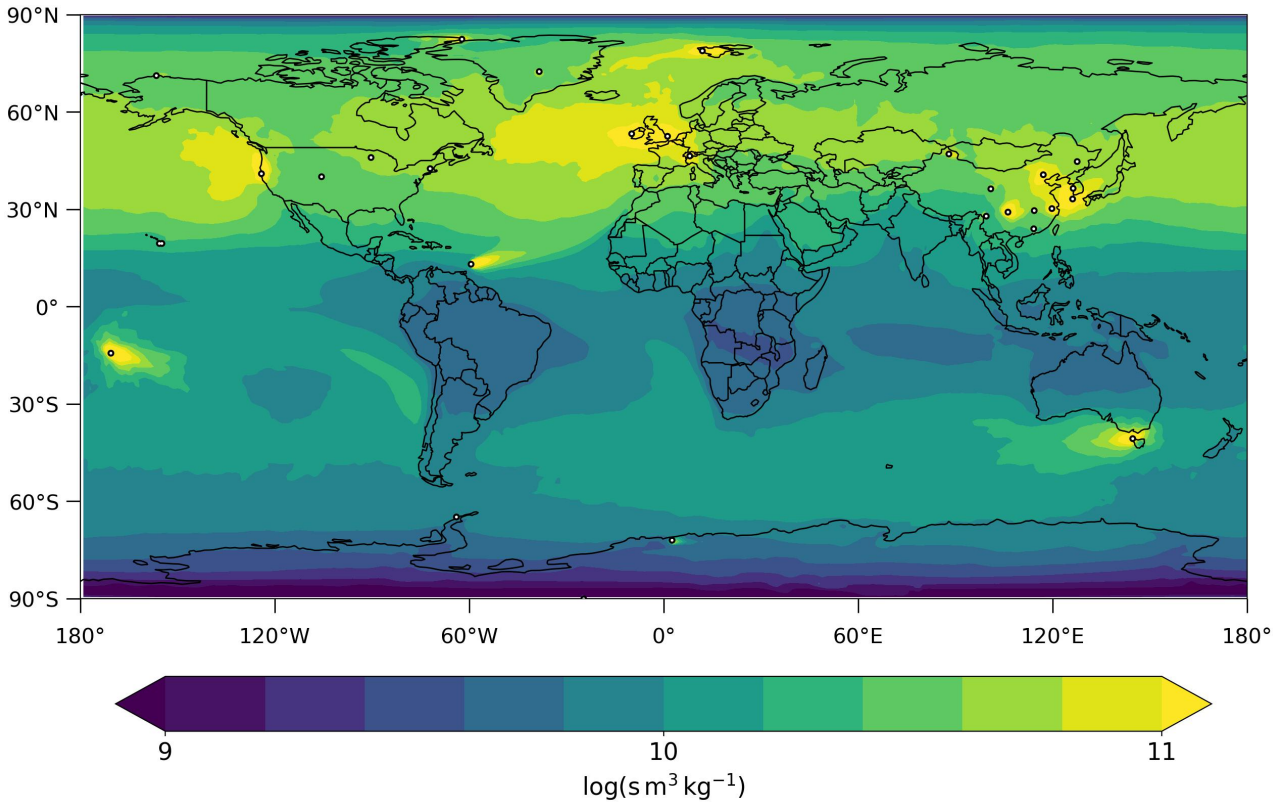

Fig. 5 Source-receptor relationship SRR obtained with FLEXPART backward runs for the sample year 2019. The contours represent the sensitivity of measurements to emissions in $\log(\mathrm{s\,m^3\,kg^{-1}})$, where higher values indicate well constrained regions by the observational network. The northern hemisphere exhibits high sensitivities, particularly in East Asia and Europe, while the tropics are less constrained, most notably in India and Southeast Asia.

The SRR is then derived by determining the time particles spend per day in each grid cell of the 1° x 1° output grid within the lowest 100 m above the surface, as emissions are assumed to only occur at ground level. Fig. 5 presents the global sensitivities to emissions for the year 2019. Close to measurement sites, sensitivities are highest, while regions further away, most notably South America, Africa, and the Indian subcontinent, exhibit lower sensitivities. The annual-mean sensitivities suggest that emissions from all grid cells contribute to modelled mixing ratios, but this does not imply that actual emissions from every region can be resolved at all times. If particle trajectories fail to reach a given location during specific periods, emissions from that region may remain unconstrained. To address this issue, emissions are stabilised with the prior estimate and only optimised annually, ensuring robust results. Also note that

fig. 5 uses a logarithmic scale to account for the rapid decrease in emission sensitivity with increasing distance from measurement sites. Additionally, regions around flask stations exhibit lower sensitivity due to their infrequent sampling intervals.

3.4. Baseline estimation with reanalysis simulation

As mentioned in the previous section, the transport model only accounts for emissions occurring during the 100 d backward simulation period. However, emissions prior to this period (background emissions) also influence measured mixing ratios and must be included in the inversion. This is achieved implicitly by introducing a baseline of atmospheric mixing ratios, obtained using the global-distribution-based (GDB) method where a sensitivity at the termination point of each particle trajectory is multiplied with the mixing ratio of C_2F_6 at that spatio-temporal location. The termination sensitivities of each backward simulation are saved on a 1° x 1° grid on 12 vertical levels with upper boundaries at 0.1, 0.5, 1, 2, 3, 5, 7, 9, 12, 15, 20, 50 km and combined with a global reanalysis of C_2F_6 mixing ratios. Mathematically, this approach can be described by dividing the forward model into the already discussed direct contribution ($\mathbf{H}_e\boldsymbol{x}_e$) from emissions within the backward period and the initial contribution ($\mathbf{H}_i\boldsymbol{y}_i$) from the baseline:

$$\boldsymbol{y} = \mathbf{H}\boldsymbol{x} = \mathbf{H}_e\boldsymbol{x}_e + \mathbf{H}_i\boldsymbol{y}_i, \tag{5}$$

where $\mathbf{H}_i$ represents the termination sensitivity applied to the vector $\boldsymbol{y}_i$, containing the global mixing ratio field, to obtain the initial contribution from outside the 100 d simulation period. To reduce the dimensionality of the problem, the baseline is aggregated into 8 latitudinal bands, 1 vertical level and a temporal resolution of 30 d. The complete state vector $\boldsymbol{x}$ is constructed by concatenating direct emissions and the aggregated baseline, while concatenating the termination sensitivity and the SRR forms the complete atmospheric transport operator $\mathbf{H}$ (for more detail, see Thompson and Stohl (2014) sec. 2.3). During the inversion, the complete state vector is estimated, optimising both direct emissions and the baseline. This method is applied to correct potential biases in the baseline introduced by possible errors in the reanalysis simulation. In general, the GDB method for baseline estimation is advantageous compared to alternative observation-based methods as it is able to account for meteorological variability, among other benefits(Thompson & Stohl, 2014; Vojta et al., 2022).

There is no publicly available reanalysis of atmospheric C_2F_6 mixing ratios that could be used for baseline estimation; therefore, a custom global 3D simulation was performed specifically for this study. The reanalysis is obtained using the Linear Chemistry Module (LCM) of FLEXPART version 11 (Bakels et al., 2024) where the LPDM operates in a forward domain-filling mode. LCM is based on the FLEXPART Chemical Transport Model (CTM) (developed by Henne et

al. (2018) and described by Groot Zwaaftink et al. (2018)) and improves upon its predecessor by calculating tracer mixing ratios via direct division of tracer mass by air mass, rather than by air density and volume. FLEXPART-CTM introduced noise in the output and led to spurious accumulation of particles, which has been mitigated in the latest version (Bakels et al., 2024). In FLEXPART-LCM, 50 million particles are released, each carrying a virtual mass which is used to produce daily mixing ratio fields on a 3° x 2° output grid on 10 vertical levels with upper boundaries at 0.1, 0.5, 1, 3, 5, 7, 10, 15, 25 and 40 km above the ground. Particle masses are initialised using a latitudinal profile of atmospheric mixing ratios to reduce the spin-up time. The latitudinal profiles are derived from interpolation between background measurements within a 30 d window around the simulation start date (Vojta et al., 2022). Ideally, a single simulation would be performed for the entire study period, but computational constraints necessitated annual subdivisions with each year simulated in parallel. This approach required reinitialization and a repeated two-month spin-up period for each year.

To account for emissions occurring during the simulation period (2003-2023), LCM does not release new particles, but instead adds emitted mass in a given grid cell to passing particles near emission sources (Bakels et al., 2024; Groot Zwaaftink et al., 2018). Emission data was based on a scaled version of the EDGARv8.0 BU inventory, with emissions in India and South Korea scaled to the average between EDGAR estimates (EDGAR, 2023) and the national inventories reported to the UNFCCC (UNFCCC, 2024b). The resulting global emissions were further scaled to match TD estimates derived from a global two-dimensional 12-box model, as reported by Rigby et al. (2014) and Say et al. (2021). The scaling of the EDGAR estimate is motivated by unrealistically low emissions in South Korea and India and the general large discrepancy to global TD estimates. Biases in the emissions provided to the reanalysis simulation would propagate into the baseline, thereby affecting global posterior emissions, leading to over- or underestimation depending on the baseline bias.

To further reduce possible errors and biases in the reanalysis, a simple data assimilation technique was used which nudges modelled mixing ratios towards measurements when particles reside within a specified spatio-temporal kernel around measurement locations. The nudging tendency or nudging increment Δm_{ij} for each particle (j) - measurement (i) pair is added to the simulated mass and is given by (Groot Zwaaftink et al., 2018):

$$\Delta m_{ij} = w_{s,ij} w_{t,ij} \frac{M_i - m_j}{\tau} \Delta t, \tag{6}$$

where $M_i - m_j$ represents the deviation between simulated particle mass (m_j) and measured mass (M_i). τ is the nudging relaxation timescale and Δt is the model synchronization time step. To ensure numerical stability, Δt is set to 900 s and τ to 1800 s. $w_{s,ij}$ and $w_{t,ij}$ represent a spatial (s) and temporal (t) weight depending on the distance between each particle-measurement pair and are defined as:

$$w_{s,ij} = \left(1 - r_{ij}^2\right) I,\ I = \begin{cases} 1 & \text{if } r_{ij}^2 < 1 \\ 0 & \text{otherwise} \end{cases}, \tag{7}$$

where r_{ij}^2 follows:

$$r_{ij}^2 = \left(\frac{x_j - x_i}{h_x}\right)^2 + \left(\frac{y_j - y_i}{h_y}\right)^2 + \left(\frac{z_j - z_i}{h_z}\right)^2, \tag{8}$$

and

$$w_{t,ij} = \left(1 - \left|\frac{t_j - t_i}{h_t}\right|^3\right)^3. \tag{9}$$

x_j, y_j, z_j, and t_j refer to the particle's location and the current model time; x_i, y_i, z_i, and t_i refer to the measurement's location and sampling time. To adjust the impact of each individual observation station on the modelled mixing ratio field, h_x, h_y, h_z, and h_t are introduced which define the spatio-temporal kernel extents in which particles are nudged. In this study, kernel sizes were chosen based on the variability of measured mixing ratios and ranged between 1° - 8° in horizontal, 100 m - 1000 m in vertical and 1 d - 10 d in temporal extent. Stations with smaller kernel extents were mainly situated in East Asia due to their proximity to emission sources. For the year 2019, a test run was performed where nudging was disabled at stations ALT, GSN, HFM, KUM, LAN, LFS, MLO, NWR, TAC and TRL to use these for validation of modelled against measured mixing ratios. In the final reanalysis used for baseline calculation, nudging was activated for all stations.

Additionally, two FLEXPART-CTM simulations were performed for 2019 using the exact same settings as the validation and the full FLEXPART-LCM runs. Results of both models are compared in sec. 4.2.

3.5. A priori emissions

In most regions of the domain, the Emissions Database for Global Atmospheric Research (EDGAR) F-GASES version 8.0 emission inventory (EDGAR, 2023) serves as the prior emission information for the inversion. This inventory is compiled exclusively using BU methods, combining industry activity data with sector-specific emission factors. According to Olivier (2022), EDGAR derives total PFC emissions for Annex-I countries and electronics industry emissions for Non-Annex-I countries from reports submitted to the UNFCCC (UNFCCC, 2024a, 2024b). Emissions from primary aluminium production are reportedly based on data from the IAI (IAI, 2021). However, comparisons between EDGAR and original UNFCCC reports reveal significant

discrepancies across all countries, with particularly large deviations in some cases. As a result, the precise methodology underlying EDGAR's estimation of C_2F_6 emissions remains unclear. Despite these uncertainties, EDGAR remains the only available global gridded BU inventory and is therefore used to construct the prior. However, adjustments were made for China, South Korea, and India, where EDGAR's estimates appear unrealistic and would otherwise impact posterior emissions. These adjustments were based on alternative BU datasets, following the requirement that prior information should be independent of observations used in the inversion. In cases where data gaps existed for certain years, emissions were linearly interpolated or extrapolated based on adjacent trends.

China

Guo et al. (2023) compiled an independent BU inventory for several F-gases in China, including C_2F_6, using detailed industry data. Their estimates are up to 5 times higher than EDGAR's and up to 3 times larger than those reported by China to the UNFCCC (Ministry of Ecology and Environment, 2018, 2024). The findings of Guo et al. (2023) also align more closely with two regional TD studies in China (An et al., 2024; Kim et al., 2021). However, as this dataset lacks spatially resolved gridded emissions, the spatial distribution from EDGAR was retained and scaled to the average of the country total reported by Guo et al. (2023) and EDGAR. Particularly from 2010 onwards, this approach results in an overall increase in prior emissions and captures a strong trend of rising C_2F_6 emissions in China, which is consistent with the expansion of the aluminium and semiconductor industries (British Geological Survey, 2025; Choi, 2023).

South Korea

In South Korea, EDGAR estimates C_2F_6 emissions between 0.1 and 3.5 t/y, significantly lower than the country's own UNFCCC report estimating emissions between 20 and 120 t/y (UNFCCC, 2024b). These higher estimates are further supported by a TD study by Kim et al. (2021), who present similar magnitudes. Although South Korea's emissions are well constrained by observations, using an unrealistically low prior such as the EDGAR dataset could artificially restrict the magnitude of the inversion increment, depending on the assumed uncertainty. To ensure more realistic posterior emissions, EDGAR's spatial distribution was preserved, but scaled to the average of EDGAR and UNFCCC values for each year. This modification provides the inversion more freedom while taking both inventories into account.

India

Similar to South Korea, EDGAR's C_2F_6 emission estimates for India are unrealistically low, ranging from 6 to 12 t/y, while UNFCCC reports indicate emissions up to 100 times higher. Assuming the reported estimates are accurate, India's industries would account for up to 50%

of global TD emissions. However, assuming that India's electronics industry emissions are likely much smaller than the aluminium industry's emissions, and given that the country produces only $\approx 6\%$ of the world's primary aluminium, the UNFCCC values appear unreasonably high. An additional problem arises from a lack of observational constraint in India, as the measurement dataset does not include Indian stations, and natural barriers such as the Himalayas and Tibetan Plateau limit transport of air masses originating from India to the Chinese network. Using high prior emissions with realistic uncertainties could lead to large adjustments in the posterior, introducing instability in the inversion, as observed in test simulations using UNFCCC data as the prior.
The recently published India Fourth Biennial Update Report to the UNFCCC (MoEFCC, 2024) for 2020 seems to utilise a revised calculation method, reporting emissions of 273 t/y - approximately a quarter of the emissions reported for 2016 - despite an increase in aluminium smelting and no significant emission mitigation efforts during that period (British Geological Survey, 2025; Indian Bureau of Mines, 2025). Assuming a negligible contribution of other source industries, the 2020 value was extrapolated to all other years using primary aluminium production data from British Geological Survey (2025). The final prior then used in the inversion was derived as the average between this extrapolated UNFCCC-based estimate and EDGAR's values. This approach yields a BU inventory for India that is approximately 10% of the estimate by Guo et al. (2023) for China, consistent with the ratio of Indian to Chinese aluminium production (British Geological Survey, 2025). Note that this inference carries substantial uncertainty, as - contrary to India - a significant portion of Chinese C_2F_6 emissions originate from the semiconductor industry.

Initial inversion tests using the adjusted EDGAR prior emissions yielded more stable and robust results, with the global sum aligning well with estimates from the AGAGE 12-box global model (see sec. 5.3) (Rigby et al., 2014; Say et al., 2021).
The EDGAR dataset and most reports to the UNFCCC do not include emission uncertainty estimates. However, the 2019 Refinement to the 2006 IPCC Guidelines for National Greenhouse Gas Inventories (Calvo Buendia et al., 2019), which underlies all BU datasets used in this study, provides uncertainty ranges for the electronics and metal industry emissions. Generally, activity data uncertainties are significantly lower than those associated with emission factors, although specific uncertainty ranges strongly depend on industry type and applied technology. Taking into account the various uncertainty estimates provided by Calvo Buendia et al. (2019) and the deviations between BU estimates and previous TD studies (An et al., 2024; Kim et al., 2021; Say et al., 2021), an uncertainty of 100% was assigned in each grid cell, with a minimum uncertainty of $10^{-15}\,\mathrm{kg/h/m^2}$ to give the inversion the possibility to correct potentially missing emissions in the prior field.

3.6. Inversion algorithm FLEXINVERT+

The Bayesian inversion framework FLEXINVERT+, developed and described in detail by Thompson and Stohl (2014), combines prior emissions (sec. 3.5), the baseline (sec. 3.4), measurements (sec. 3.2) and the SRR (sec. 3.3) to provide the optimal estimate of posterior emissions according to Bayes' theorem. The algorithm calculates the analytical solution to the cost function for the posterior state (eq. 3) and the posterior error estimate (eq. 4). To minimise computational cost while retaining critical emission information, a grid with variable resolution is introduced for the emission field during optimisation. Starting with a coarse grid at an 8° x 8° resolution, grid cells at locations with strong observational constraints or high prior emissions are subdivided into 4, 16, or 64 finer grid cells, yielding resolutions of 4° x 4°, 2° x 2°, or 1° x 1°, respectively. This variable grid is produced once, using the SRR and emission data from 2019, and applied to all years. All ocean grid cells as well as Antarctica are excluded from the grid, as no emissions are expected from these regions. This dimension reduction method decreases the number of grid cells from initially 64,800 (with a 1° x 1° resolution) to 7,789, thus enhancing computational efficiency while preserving high resolution in key areas. The temporal resolution is set to 1 yr, as prior emissions are only available annually and the number of measurements is relatively limited. Although the ideal approach would be to solve the inversion in a single simulation with $\boldsymbol{y}$ containing all measurements and $\boldsymbol{x}$ containing emission grid cells for all years, this is impractical due to the need to invert and store large matrices. Instead, the inversion is performed separately for each year, allowing parallel computation. The complete state vector $\boldsymbol{x}$ for each year is constructed by concatenating the baseline with the variable grid emissions. The dimension of each state vector is therefore 7,789 (variable grid) + 104 (baseline) = 7,893, whereas the dimension of each observation vector $\boldsymbol{y}$ is equal to the number of 3 h averaging intervals around measurements in each year, ranging from 2,798 to 16,631.

Prior error covariance matrix B

The prior error covariance matrix contains the uncertainties associated with prior emissions and the baseline along the diagonal, with off-diagonal elements representing correlations between grid cells. The emission uncertainty is assumed to be at 100% of the prior emissions (see sec. 3.5), while the baseline uncertainty is set at 0.1 ppt, based on the validation reanalysis simulation. Spatial correlation is considered using an exponential decay with a scale length of 100 km, reflecting the relatively localized nature of emission correlations in industrial regions. Temporal correlations are not considered, as annual emissions are estimated separately. Due to limited information, the baseline is assumed to be uncorrelated, although this assumption may not be entirely accurate (Thompson & Stohl, 2014).

Observation error covariance matrix R

The observation error covariance matrix accounts for errors in the observation space, including uncertainties from measurements, model transport, and representation errors. Measurement errors associated with the measuring systems, reported by observation network operators, are usually around 0.05 ppt, which is relatively small compared to the assumed model and representation errors. However, these errors are difficult to quantify, as they depend on multiple factors in the atmospheric transport model, for which uncertainty assessment is in theory possible using ensemble methods, but in practice challenging to achieve (Thompson & Stohl, 2014). Therefore this study applies another method to represent such uncertainties.

To address errors of the model and its representation of the measurements, Henne et al. (2016), Bergamaschi et al. (2022) and Vojta et al. (2024) describe methods that consider the errors as deviations of measurements from modelled mixing ratios. A simplified version of their approach is adopted here, where a fixed uncertainty of 0.1 ppt is assigned to measurements below 6 ppt, while the uncertainty for measurements above this threshold increases linearly with the mixing ratios. This simplified implementation was applied, as a priori modelled mixing ratios are very smooth for C_2F_6, while observations are much more variable, especially at locations close to emission sources. The observations strongly influenced by close-by emissions are expected to not be well represented by the model. In test simulations without this adjustment, the optimised baseline exhibited an unrealistically strong variability, as both very high and low measurements impacted the baseline equally. The observation error covariance matrix $\mathbf{R}$ is assumed to be diagonal, neglecting potential correlations between observations and model representations due to a lack of available information on such correlations.

FLEXINVERT+ outputs the posterior emissions and uncertainties on both the regular 1° x 1° grid as well as on the variable grid for further analysis and post-processing, as discussed in the next section.

3.7. Emission constraints and post-processing

Inversions of C_2F_6 suffer from a particularly sparse observational network, resulting in weak constraints, particularly over tropical and Southern Hemisphere land areas. To address issues arising from this limitation, two additional constraints are applied as post-processing steps to the analytical inversion output: 1) a constraint on total global emissions and 2) a non-negativity constraint, given that C_2F_6 sinks are negligible compared to emissions. The total global constraint is a novel method developed for this study, while the non-negativity constraint has been used for several previous works (Thompson & Stohl, 2014; Vojta et al., 2022, 2024). Both constraints are implemented using an analytical solver, similar to the approach used in FLEXINVERT+, and are formulated as follows:

$$\hat{\boldsymbol{x}} = \boldsymbol{x} + \mathbf{A}\mathbf{P}^T(\mathbf{P}\mathbf{A}\mathbf{P}^T + \mathbf{C})^{-1}(\boldsymbol{c} - \mathbf{P}\boldsymbol{x}), \tag{10}$$

where $\hat{\boldsymbol{x}}$ represents the constrained posterior emissions, $\boldsymbol{x}$ the initial posterior emission estimate, and $\mathbf{A}$ is the associated posterior error covariance matrix, as obtained from eqs. 3 and 4. The content of the matrix $\mathbf{P}$ and vector $\boldsymbol{x}$ varies depending on the applied constraint, as detailed below. The non-negativity constraint follows the method of Thacker (2007), while the total global constraint is an adaptation of this approach.

Total global constraint

To constrain the sum of posterior emissions to well-known total global emission estimates for each time step, $\mathbf{P}$ represents a matrix of ones, which sums all flux entries of the posterior state vector $\boldsymbol{x}$ for each time step to compare them to the total global values contained in $\boldsymbol{c}$. The matrix $\mathbf{C}$ is optional and contains the uncertainties of the total global emission values on its diagonal, with off-diagonal entries set to 0. If $\mathbf{C}$ is non-zero, the posterior error covariance matrix will change accordingly. However, due to the unrealistically low resulting errors of the constrained posterior, the reported uncertainties remain those of the unconstrained posterior. The ratio between posterior and total global errors determines the impact of the constraint and the regional distribution of its increment, where the constraint predominantly affects regions with high posterior uncertainties while exerting minimal influence on well-observed regions. Total global emissions and their uncertainties, represented by $\boldsymbol{c}$ and $\mathbf{C}$, respectively, are derived from AGAGE 12-box model simulations (Rigby et al., 2014; Say et al., 2021), selected for their high accuracy and robustness and are extrapolated for 2020-2023.

Non-negativity constraint

In the applied Bayesian inversion framework, uncertainties are assumed to be Gaussian distributed, which can yield negative posterior emissions in individual grid cells. Since negative C_2F_6 fluxes are known to be negligible, negative values are constrained to zero. For this non-negativity constraint $\mathbf{P}$ represents a matrix with ones at positions corresponding to negative entries in $\boldsymbol{x}$, while $\boldsymbol{c}$ is a vector containing zeros for every negative value. $\mathbf{C}$ is 0, as there is no uncertainty in the non-negativity constraint, leading to a formally unchanged posterior error covariance matrix (Thacker, 2007).

For further analysis of national and regional C_2F_6 emission estimates, emissions were masked according to political borders. Given the 1° x 1° resolution, emissions in grid cells overlapping multiple region's territories are apportioned based on the fractional land area of each region within the grid cell. Since emissions are highly localised and mostly concentrated at specific industrial sites which are not close to their region's borders, this issue has minimal overall impact. Prior and posterior uncertainty assessments for each region follow the approach of Henne et al.

(2016), applying a mask vector to the respective error covariance matrix and accounting for correlations between grid cells. To correctly quantify the uncertainty associated with regions containing multiple grid cells, Gaussian error-propagation was applied.

4. Global reanalysis of C_2F_6 mixing ratios

The following sections present the results of the global C_2F_6 mixing ratio reanalysis, conducted using FLEXPART-LCM, driven with ERA5 meteorological input data to simulate the release and atmospheric transport of C_2F_6 between 2003 and 2023. Measurements were incorporated to nudge the modelled fields toward observed mixing ratios, minimising overall uncertainty and bias. Sec. 4.1 presents the results of the full simulation for the sample year 2019, using all available measurements for nudging. In sec. 4.2 , LCM results are compared to its predecessor model, FLEXPART-CTM, using an additional validation setup in which one-third of all stations were excluded from the nudging process.

4.1. Spatial and temporal distribution

The mean global C_2F_6 distribution for 2019, averaged from the surface to 10 km altitude is illustrated in fig. 6. It exhibits a distinct latitudinal gradient, with lower mixing ratios in the Southern Hemisphere (SH) and higher values in the Northern Hemisphere (NH). The spatial distribution of mixing ratios closely follows the emission pattern, with the highest values simulated in China, Japan, South Korea, and Taiwan. Additional local maxima occur in regions such as eastern Quebec in Canada (Sept-Îles, Alma, Bécancour), southern Siberia in Russia (Krasnoyarsk, Bratsk) and Singapore, corresponding to locations of major aluminium smelters (Pawlek, 2023) or semiconductor manufacturing locations included in the EDGAR emission dataset, provided to LCM. Exceptionally high C_2F_6 mixing ratios in India can most likely be attributed to overestimated emissions in the UNFCCC-scaled EDGAR dataset. In India, the original EDGAR dataset underestimated emissions from several known aluminium smelting sites (Korba, Jharsuguda, Angul; Pawlek (2023)), requiring the application of a national correction factor based on UNFCCC reports. However, these earlier reports likely overestimated emissions as indicated by the latest Indian UNFCCC report (MoEFCC, 2024), which was only published after the reanalysis simulations were already performed. For this reason, the prior emissions used in the inversions were additionally adjusted to mitigate this overestimation (see sec. 3.5). During winter season in India, weak regional circulation and large scale high pressure systems result in the accumulation of pollutants, including C_2F_6, near the surface (Sharma & Mauzerall, 2021). Despite these regional discrepancies, the global mean mixing ratio is likely very close to reality, owing to the accurate total global emission magnitude.

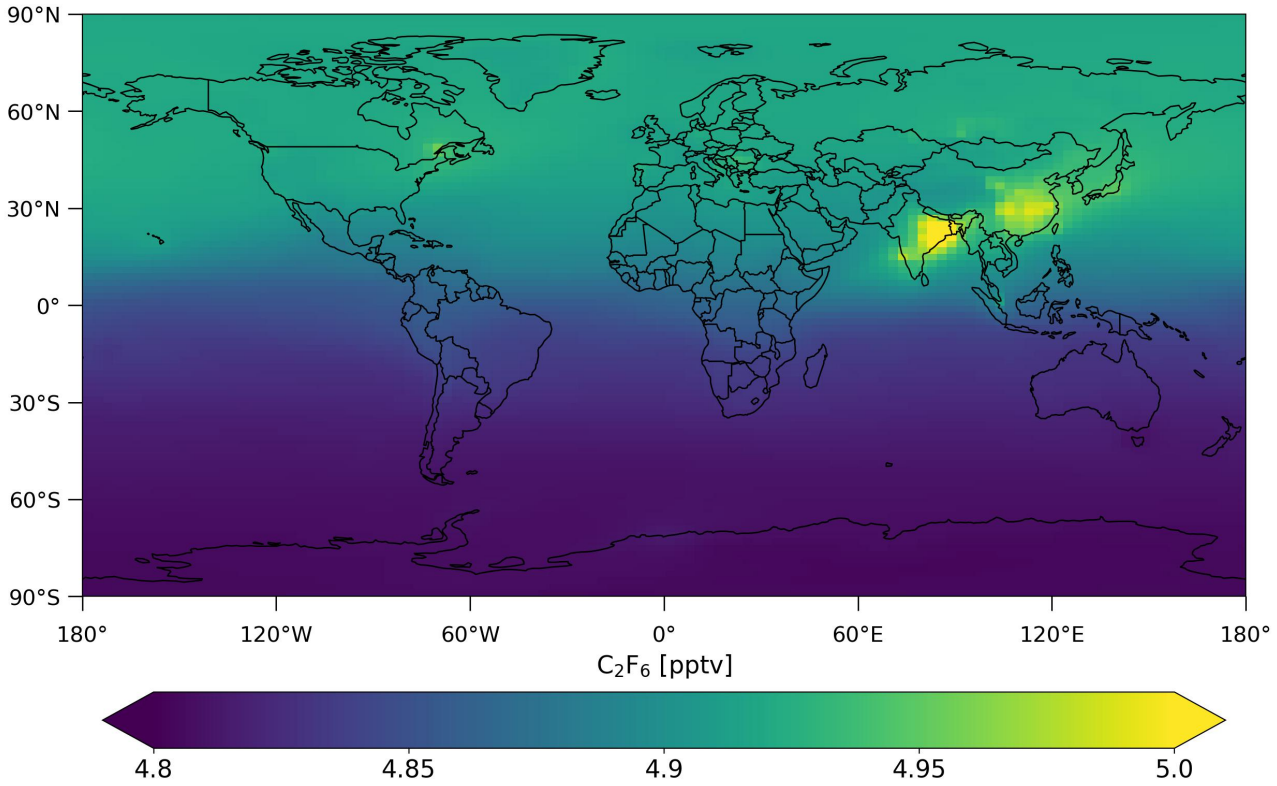

Fig. 6 Annual mean global C_2F_6 mixing ratio distribution in 2019 from FLEXPART-LCM. Highest values are simulated in regions with large aluminium smelting or semiconductor manufacturing industries (East Asia, India, Canada, Russia)

The vertical gradient of C_2F_6 mixing ratios varies by latitude, as shown in fig. 7. In the NH, where nearly all emissions occur, the mixing ratio decreases with altitude due to the vertical transport of surface emissions towards the tropopause. In the extratropics (30°N-90°N), vertical transport dominates over meridional transport, resulting in a relatively weak vertical gradient up to the tropopause. In contrast, averaged over a year, cross-equatorial transport plays a greater role than vertical transport in the tropics (0°-30°N), reducing upper troposphere mixing ratios and establishing a strong vertical gradient.

However, seasonal variability significantly influences vertical profiles in the NH tropics (not shown in fig. 7). During summer, convection-driven vertical mixing reduces the gradient to near zero, whereas in winter, weak upward motion or even subsidence leads to a strong decrease in mixing ratios with altitude. In the SH, where surface emissions are negligible, meridional transport from the NH at high altitudes results in a positive vertical gradient toward the tropopause. This effect is more pronounced in the tropics (30°S-0°) than in the extratropics (90°S-30°S), mirroring the pattern in the NH. Minor sources in the SH extratropics possibly reduce the vertical gradient further. Given a global C_2F_6 growth rate of 0.09 ppt/y in 2019 (Say et al., 2021), transport from the NH surface to the SH extratropics surface takes approximately 1 y. Stratospheric mixing ratios remain much lower than tropospheric values, as transport across

the tropopause is slow and occurs primarily in the tropics. Note that the tropopause-induced negative gradient occurs at lower altitudes in the extratropics ($8 - 10$ km) compared to the tropics ($12 - 16$ km), consistent with regional tropopause heights.

A key advantage of the GDB baseline estimation approach over statistical selection-based methods is evident in fig. 8. The figure illustrates the temporal evolution of a latitudinal C_2F_6 profile from the validation run averaged over 122°E-131°E and the lowest 3 model layers ($0 - 1$ km). There are three nudging stations located within this area, Longfengshan (LFS, 44.7°N, 127.6°E), Anmyeon-do (AMY, 36.5°N, 126.3°E) and Gosan (GSN, 33.3°N, 126.2°E). The seasonal oscillation of the Inter-Tropical Convergence Zone (ITCZ), representing the border between high NH and low SH mixing ratios, is evident around the equator with air masses of the opposing hemisphere extending north or south during the respective hemisphere's summer season. Occasionally, SH air masses are transported to extratropical latitudes, as observed at GSN between July and August 2019. This intrusion of less polluted air during NH summer in the model can be validated with lower-than-usual C_2F_6 measurements at this station (fig. 9, further discussions in sec. 4.2). Such a feature could not be accurately captured using other baseline estimation methods (see also Vojta et al. (2022) and Vojta et al. (2024)).

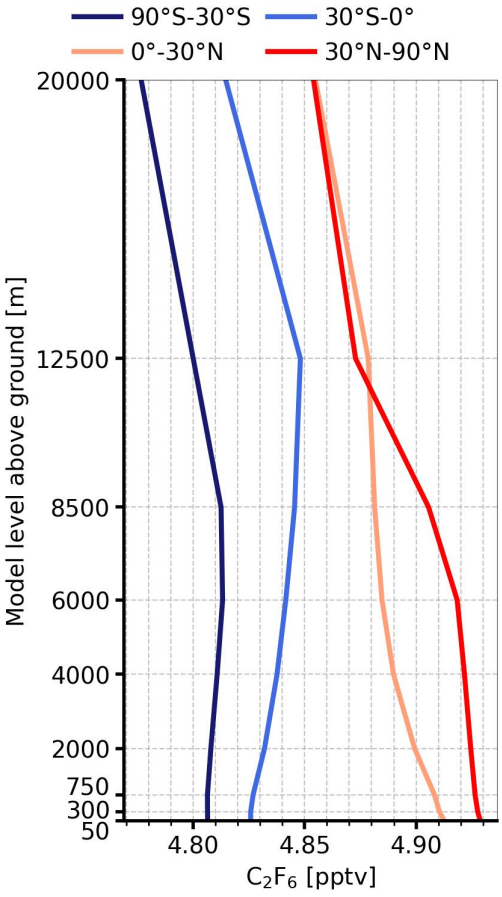

Fig. 7 Vertical C_2F_6 mixing ratio profiles, averaged over 2019, for SH extratropics (90°S-30°S, dark blue), SH tropics (30°S-0°, light blue), NH tropics (0°-30°N, orange) and NH extratropics (30°N-90°N, red). As emissions primarily originate from the NH, vertical gradients are negative in the NH and positive in the SH.

Between 40°N and 50°N, nudging to measurements at LFS occasionally introduces much lower (end of August) or higher (beginning of October) mixing ratios, as measurements appear more variable than the modelled values. The subsequent meridional advection of adjusted mixing ratios appears as northward- and southward-extending peaks and troughs in fig. 8. For the nudging technique to effectively reduce global-scale biases, large kernel sizes are necessary. However, a side effect of such large kernel sizes is the smoothing of local variability otherwise captured by the model, as seen in the 40°N to 50°N region. Since reducing global bias is crucial for deriving a reliable baseline, larger kernel sizes are preferable, particularly when using long 100 d backward simulation periods.

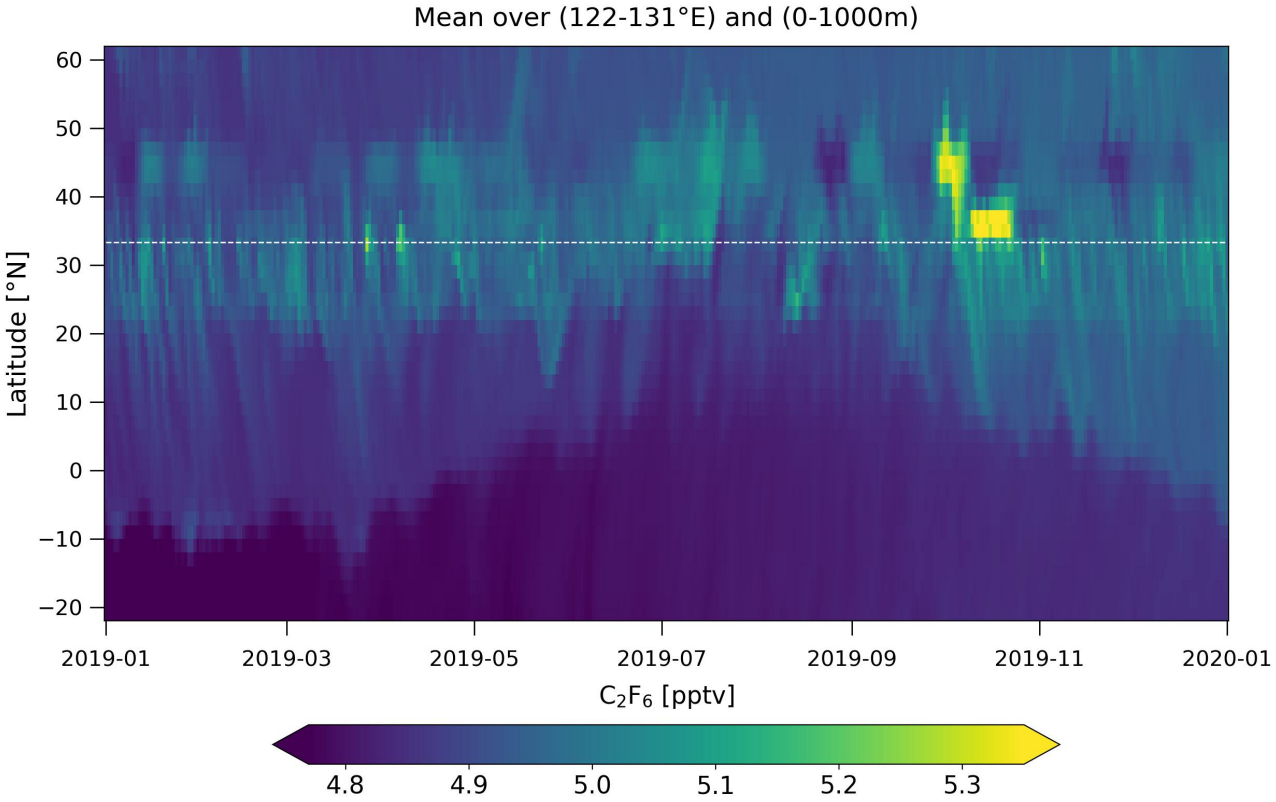

Fig. 8 Temporal evolution of a meridional mixing ratio section averaged over 122°E - 131°E zonally and 0 m - 1000 m vertically. The seasonal ITCZ oscillation is apparent around the equator transporting clean SH air masses to NH tropical and extratropical latitudes in summer. The dashed white line represents the latitude of the GSN station to compare with measurements in fig. 9.

4.2. Nudging impact and comparison of FLEXPART-LCM to FLEXPART-CTM

The nudging routine implemented in LCM and its predecessor CTM adjusts modelled mixing ratios toward observed values within a predefined 4-dimensional kernel. The kernel size varies based on measurement variability at each site. At background stations with low variability, kernel sizes of 8° horizontal, 1 km vertical and 10 d vertical extent are used, ensuring that the modelled mixing ratios correspond more closely to the observed values in a large area around the site. However, at stations near emission sources, where mixing ratios exhibit high variability, kernel sizes are reduced to 1° horizontally, 100 m vertically and 1 d temporally to minimise bias in the modelled fields from small-scale effects. When the kernel size is smaller than the 3° x 2° output grid resolution, the modelled mixing ratio in a given output grid box may deviate from the measured value, as observed at the GSN and XFG stations (Figs. 9 and 10).

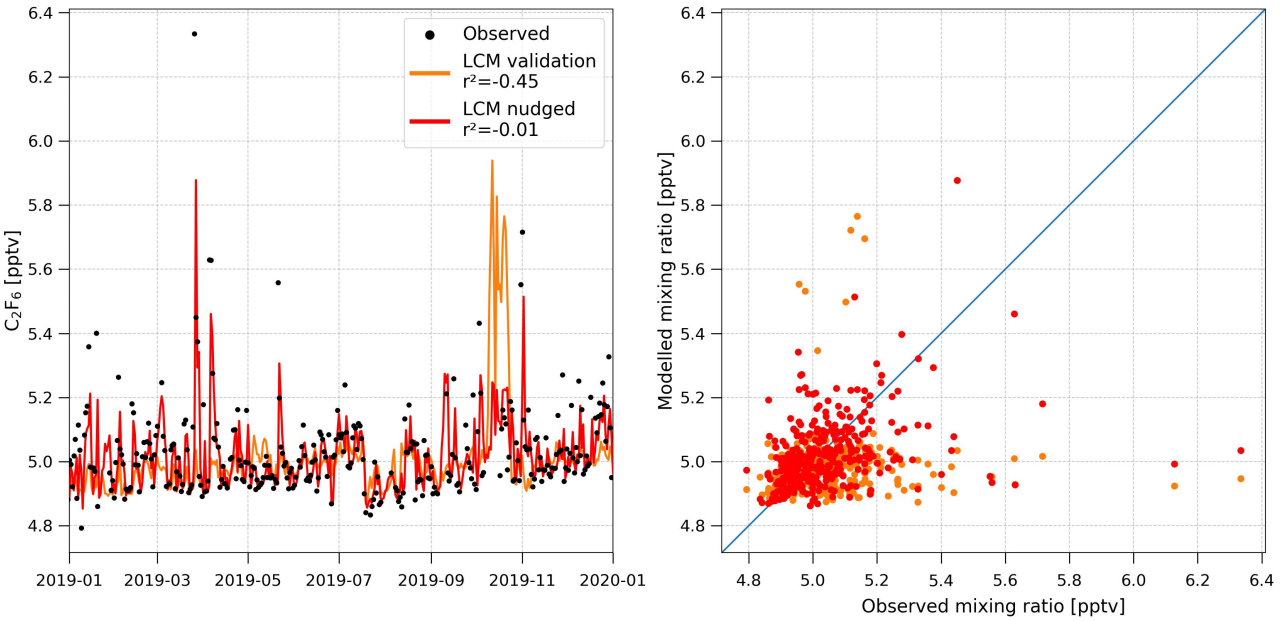

Fig. 9 GSN: Observed mixing ratios (black dots) at the measurement station in Gosan, South Korea along with modelled values of the full nudging (red) and validation (orange) LCM simulations in the corresponding grid cell (left panel). Scatter plot between measured and modelled C_2F_6 mixing ratios (right panel). While the non-nudged validation simulation exhibits reasonable agreement with measurements, the nudged simulation is able to correctly capture individual peaks.

At GSN (Fig. 9), the output of the full simulation (incorporating all stations for nudging) is compared to a validation simulation in which 10 stations, including GSN, were excluded from nudging. Compared to the validation simulation, the nudged simulation better captures individual peaks in observations, such as those in late March or early November. However, the validation simulation also demonstrates strong agreement with measurements, particularly in reproducing background mixing ratio levels. The peak in October, present in the validation simulation but absent in observations and the full simulation, results from nudging to the nearby AMY station, suggesting an overly large kernel size at AMY. This feature highlights a limitation of the simple nudging approach, which strongly depends on user-defined parameters. Activating nudging to the GSN station measurements significantly reduces modelled mixing ratios in October towards the measurements. An important feature (previously discussed in sec. 4.1, fig. 8) is the intrusion of less polluted SH air masses over GSN from July to August. The successful representation of this event in both the full and the validation simulation highlights the advantage of the GDB method for baseline estimation in inverse modelling.

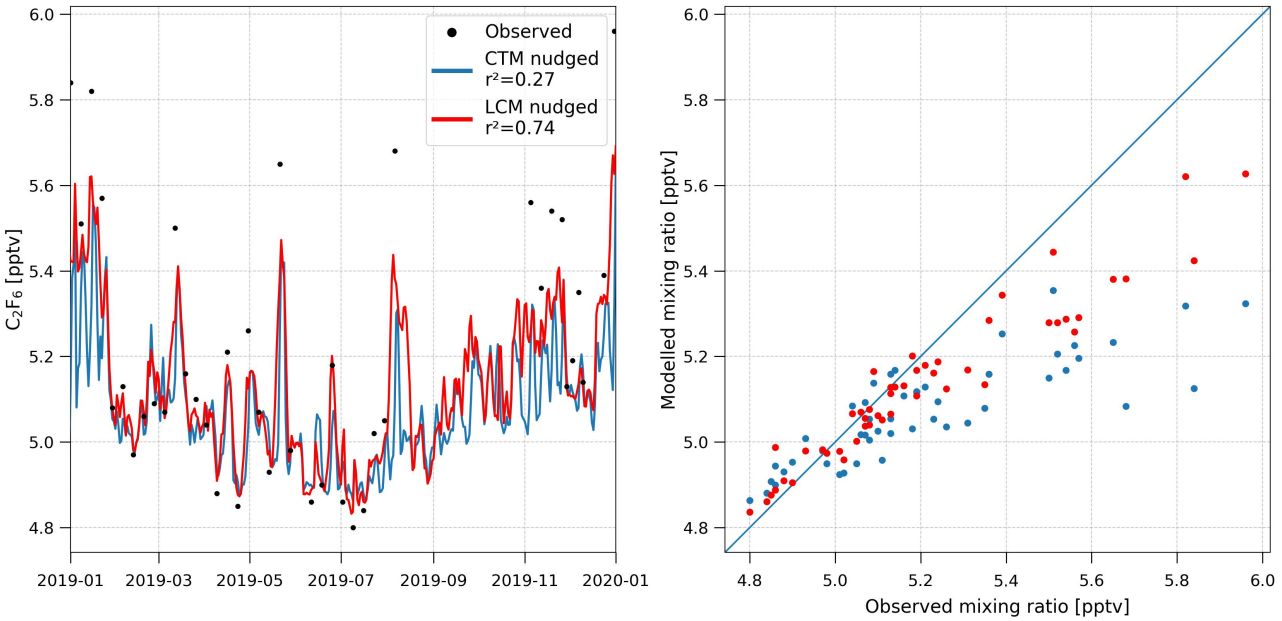

Fig. 10 XFG: Observed mixing ratios (black dots) at the measurement station in Xinfeng, China along with modelled values from LCM (red) and CTM (blue) in the corresponding grid cell (left panel). In both models, modelled fields were nudged to the XFG station's measurements. Scatter plot between measured and modelled C_2F_6 mixing ratios (right panel). CTM exhibits greater variability when nudged to high measurements, leading to larger bias than LCM, particularly at high values.

To illustrate the improvement of LCM over its predecessor CTM, modelled mixing ratios at the nudged XFG station are compared in fig. 10. While both models generally yield similar results, CTM exhibits greater variability around high-measurement events (e.g. January, November). This increased variability results in higher bias in CTM compared to LCM at such high measurements, as illustrated in the scatter plot (right panel of fig. 10). The improved performance of LCM results from improved handling of overlapping kernels and a revised method for calculating output mixing ratios, as detailed by Bakels et al. (2024).

An overview of model performances at all validation stations in the validation run is summarised in tab. 2. At 6 out of 10 stations, LCM outperforms CTM in terms of both bias (ME) and accuracy (RMSE), while 2 stations show improvement in only one metric. However, at LFS and TAC, LCM exhibits poorer performance than CTM, although the underlying causes remain unclear. Overall, differences between the two models are generally small, with deviations on the order of a few percent in most cases.

At stations located near emission sources (e.g. GSN and LAN), models struggle to capture the full variability and magnitude of the measurements. At most background stations, LCM exhibits a negative bias of approximately 0.025 ppt, while the RMSE is also lower, remaining below 0.1 ppt. The uncertainty estimate of the baseline in the inversion was chosen according to the RMSE and set to 0.1 ppt to account for the higher uncertainty in emission source regions.

Mean Error (Bias)

	ALT	GSN	HFM	KUM	LAN	LFS	MLO	NWR	TAC	TRL
LCM	-0.022	-0.054	-0.014	-0.071	-1.368	-0.023	-0.024	-0.035	0.023	-0.031
CTM	-0.022	-0.065	-0.013	-0.073	-1.404	-0.021	-0.029	-0.037	0.019	-0.031

Root Mean Square Error

LCM	0.058	0.191	0.084	0.087	3.394	0.096	0.079	0.061	0.036	0.071
CTM	0.059	0.178	0.086	0.089	3.408	0.096	0.081	0.066	0.032	0.072

Percentage improvement (CTM-LCM)/CTM

ME	1.2	17.3	-2.9	2.7	2.5	-5.0	19.2	7.9	-18.0	0.2
RMSE	0.1	-7.1	2.6	1.7	0.4	-0.4	3.4	7.8	-10.6	1.0

Tab. 2 Mean Error (ME) and Root Mean Square Error (RMSE) for LCM and CTM at all validation stations, along with the percentage improvement of LCM relative to CTM, are presented. Colours are used qualitatively to indicate the magnitude and direction of the error or improvement.

5. Global and regional emissions of C_2F_6

In the following chapter, results obtained with FLEXINVERT+ are presented, analysed and compared to data from various other regional and global studies. FLEXINVERT+ optimises for the best estimate of C_2F_6 emissions based on measurements and atmospheric transport obtained with FLEXPART combined with background mixing ratios and a priori emissions. Results in observation space (modelled mixing ratios at measurement stations) are presented in sec. 5.1 to assess the model performance and which stations were most important to constrain global emissions. The simulations' outputs in state space (modelled emissions on the regular grid) are analysed in secs. 5.2 and 5.3 for individual regions, countries, or globally and compared to other TD or BU emissions inventories. This study, for the first time, presents regional TD estimates for North America, the whole of Europe, and several Asian countries outside of East Asia, as well as global estimates utilising regionally resolved atmospheric transport. Emissions are simulated between 2004 and 2023; however, depending on the observational coverage in each region, results are averaged over multiple years or not interpreted to avoid mistakenly overfitting for true signals.

5.1. Inversion results: impact and robustness

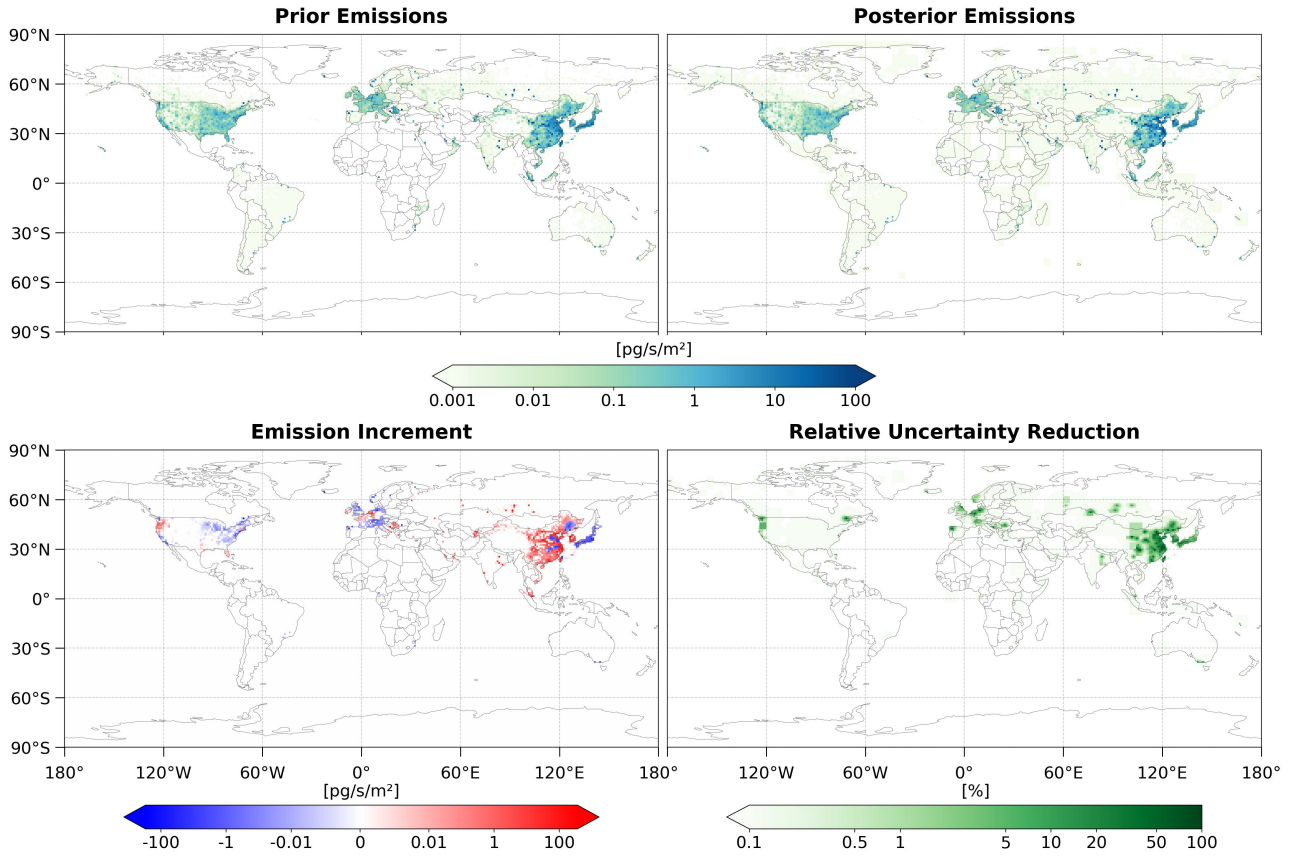

Fig. 11 Prior emissions, posterior emissions, inversion increments (posterior minus prior) and relative uncertainty reduction in 2019 (from top left to bottom right). Largest emissions, increments and uncertainty reductions are observed at a few grid cells corresponding to locations of aluminium smelting or semiconductor manufacturing facilities

An overview of the global prior and posterior emission distribution for the sample year 2019 is presented in fig. 11 (top) and shows the localised nature of C_2F_6 emissions corresponding to aluminium smelting or electronics manufacturing sites. In all years during the study period, 40 individual grid cells are responsible for >90% of global emissions, making it challenging to obtain stable inversion results and prevent overfitting. In general, the spatial distribution of the measurement-informed posterior emissions hardly differs from the prior distribution, based on the EDGAR dataset, but the emission magnitude is adjusted in key regions. This effect can be explained using the lower two maps of fig. 11, where the highest relative uncertainty reduction occurs at well-constrained high-emission locations (and highly correlating neighbouring grid cells), primarily in East Asia, Europe, and North America due to the much higher prior uncertainty assigned to those cells. This leads to larger absolute and relative increments at those locations and negligible increments in regions with low prior emissions. For the case of C_2F_6 this is desirable, as the locations of the largest emitters are generally well-known, while their

emission magnitudes are believed to be highly uncertain. The limited measurement availability for this species could otherwise lead to spurious emissions when using uniform prior emissions and uncertainties.

Fig. 11 illustrates that emissions are mainly located in East, Southeast, and South Asia (China, Japan, South Korea, Taiwan, India, Malaysia, Singapore), Europe (Germany, United Kingdom, Spain, France, Romania) and North America (Canada, USA). There are negligible emissions in South America, Africa, and Oceania compared to the other continents as the EDGAR estimate exhibits low emissions and therefore the inversion is not given much freedom in addition to lower SRR values. This means that if EDGAR were to underestimate true emissions in those regions, the posterior emissions would also be too low and the inversion does not sufficiently correct the estimate. Another feature apparent in the emission increment map of fig. 11 is a dipole between western and eastern North America, which is observed in most years of the study period. The reason is likely the sensitivity of the European stations, which measure lower mixing ratios, to the emissions in eastern North America, and of Trinidad Head (THD) and other stations in the USA, measuring higher mixing ratios, to the emissions in western North America.

	JGJ	LAN	JSA	XFG	SDZ	GSN	WLG	LFS	THD	MHD	HFM	LEF	TAC	JFJ	SUM	RPB	SMO	CGO
Posterior-Baseline [pptv]	0.48	0.46	0.35	0.34	0.20	0.14	0.14	0.11	0.06	0.05	0.05	0.05	0.04	0.04	0.04	0.03	0.01	0.00
$RMSE_{pri}$ [pptv]	1.35	2.46	0.35	0.31	0.70	0.19	0.56	0.11	0.05	0.05	0.12	0.07	0.04	0.04	0.11	0.03	0.03	0.03
$RMSE_{pos}$ [pptv]	1.23	2.32	0.24	0.21	0.63	0.14	0.53	0.10	0.04	0.04	0.11	0.06	0.04	0.03	0.09	0.03	0.03	0.02
Relative Error Red. [%]	8.8	5.4	30.3	33.6	9.5	30.0	5.1	8.4	19.3	12.7	11.1	13.0	14.7	8.2	12.2	7.4	6.2	20.4
ME_{pri} [pptv]	-0.63	-0.96	-0.24	-0.23	-0.22	-0.09	-0.26	-0.04	-0.02	-0.01	-0.07	-0.03	-0.02	-0.01	-0.07	-0.01	-0.00	0.00
ME_{pos} [pptv]	-0.34	-0.68	-0.07	-0.04	-0.13	-0.02	-0.19	0.00	-0.00	-0.00	-0.05	-0.01	0.00	0.01	-0.05	0.01	0.00	-0.00
r^2_{pri}	0.02	0.03	0.30	0.41	0.08	0.22	0.04	0.13	0.14	0.28	0.15	0.33	0.29	0.58	0.09	0.44	0.42	0.22
r^2_{pos}	0.04	0.06	0.41	0.47	0.20	0.50	0.03	0.18	0.30	0.41	0.22	0.32	0.41	0.60	0.19	0.54	0.44	0.42

Tab. 3 Performance metrics of modelled prior and posterior mixing ratios at 18 observation stations for all available measurements in the study period. Individual stations are ordered according to the average difference between baseline and posterior mixing ratios, indicating influence of measurements by emissions 100 d prior to sampling. r^2 describes coefficient of determination between linearly detrended measured and modelled values. Colours are used qualitatively to indicate the magnitude and direction of the metric.

An overview of several performance metrics of prior and posterior modelled mixing ratios compared to observations at measurement stations for the whole study period is given in Tab. 3. Shown are the 16 stations with the largest influence of the emissions during the 100 d backward

simulation period, determined in terms of the average difference between the posterior baseline and posterior mixing ratio. Additionally, the two background stations Cape Matatula (SMO) and Cape Grim (CGO) are presented where the posterior magnitude is nearly identical to the baseline to illustrate the optimisation effect at various measurement locations. The stations with the 8 largest deviations of posterior mixing ratios from the baseline are situated in East Asia, followed by stations in the US and western Europe. As expected, stations at remote locations are minimally influenced by emissions during 100 d prior to the sample time.

The posterior RMSE is lower than the prior RMSE at all stations, showing that the optimisation leads to more accurate posterior mixing ratios; however, both measures are much higher at East Asian stations compared to elsewhere. This is likely the result of higher variability of observed mixing ratios which is not captured by the model as atmospheric transport of narrow plumes from close-by emissions is generally less accurate. Additionally, the discrepancies between prior emissions and real emissions are likely higher, indicated by a larger bias of a priori mixing ratios. Among the East Asian stations, there are differences in the relative error reduction stemming from the formulation of the observation error, which is constant up to 6 ppt and increases linearly upwards of 6 ppt. At Jiangjin (JGJ), Lin'an (LAN), Shangdianzi (SDZ), and Mt. Waliguan (WLG), the highest mixing ratios are observed, frequently above 6 ppt, leading to a reduced impact of such measurements. This effect can be seen as a drawback of the applied observation error method, but aims at preventing overfitting of the posterior baseline which was otherwise observed. In general, error reductions are moderate, between 5% to 20% outside of East Asia. Similarly to the RMSE, the bias (ME) is also significantly reduced, indicating a better agreement of the modelled posterior with observed mixing ratio magnitudes, as expected. However, particularly the prior and to some extent the posterior are negatively biased, indicating underestimated a priori emissions. The largest bias of the posterior is observed in East Asia, particularly at stations affected by the observation error method. At most other stations, the bias of the posterior is small, at or under 0.01 ppt.

The coefficient of determination (r^2) indicates higher agreement between measurements and posterior modelled mixing ratios than prior ones, while the measure demonstrates significantly worse performance at East Asian stations than elsewhere. The outlier here is the station in Gosan (GSN), where r^2 is relatively high, likely because this station is located at the coast and receives more well-mixed air masses, leading to more accurate modelling of atmospheric transport. Overall, model performance strongly correlates with the magnitude of measured mixing ratios above the background, leading to the best performance at background stations, such as Ragged Point (RPB), SMO, and CGO. However, stations with the lowest agreement between modelled and observed mixing ratios have the largest impact on posterior emissions due to their proximity to and constraint on high-emission regions.

To compare and visualise the temporal evolution of measurements, the a priori and posteriori

baseline, and a priori and posteriori modelled mixing ratios are presented for three different stations. The station JGJ (fig. 12) exhibits very high measurements and a strong annual oscillation, GSN (fig. 13) is characterised by relatively high peaks and local minima in summer, and Mace Head (MHD) (fig. 14) displays occasional maxima when receiving polluted air masses from continental Europe, but measures mostly well-mixed background mixing ratios during periods when the air is arriving from the North Atlantic.

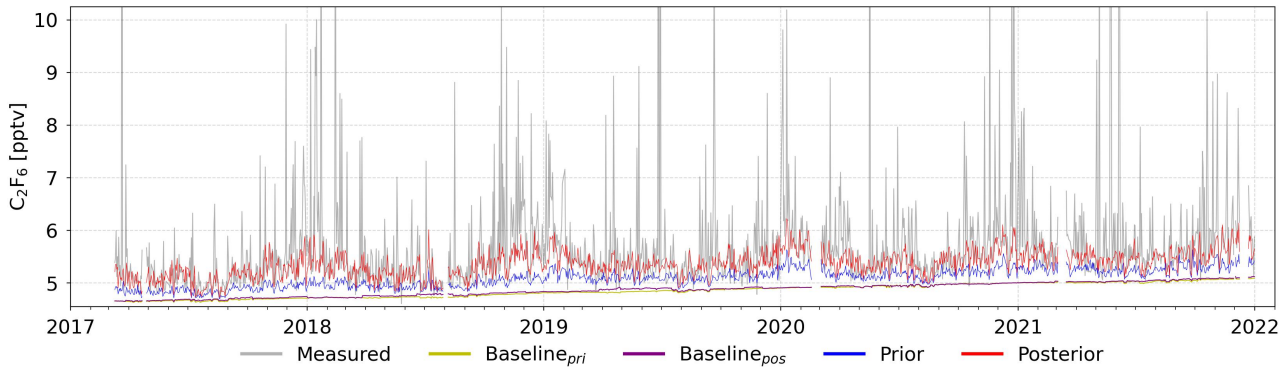

Fig. 12 JGJ: Mixing ratio time series at the Jiangjin measurement station. The grey line shows measured mixing ratios. The yellow and purple lines represent prior and posterior baselines. Blue and red lines illustrate prior and posterior modelled mixing ratios. The annual oscillation results from transport of polluted air from the north during winter and less polluted air from the south in summer.

At the JGJ station in China (fig. 12), modelled mixing ratios show the highest enhancement over the baseline of all available measurement stations, indicating particularly high influence from emissions nearby. Due to the long backward period of 100 d both the prior and posterior baseline is much lower and smoother than the measurements, as the back-trajectory termination locations are distributed nearly uniformly across the whole NH or for some cases even globally. The inversion optimises modelled mixing ratios towards the measurements, but does generally not capture high peaks due to the higher assigned observation uncertainty and the additional constraint of emissions from other stations. Difficulties in correctly modelling small scale atmospheric transport near the measurement station likely further contribute the discrepancy between modelled and measured mixing ratios.

A clear signal at JGJ is its annual oscillation apparent in measurements, where higher values occur in winter with peaks reaching upward of 10 ppt, while mixing ratios in summer are occasionally nearly as low as baseline levels. This is due to a distinct wind pattern specific to this station with prevailing northerly wind directions in winter and southerly in summer. The metropolitan area of Chongqing is situated roughly 50 km north of JGJ, and hosts a significant amount of the Chinese semiconductor industry, but it is difficult to assess the specific amount of C_2F_6 used and emitted there. Still, already a priori modelled mixing ratios capture the annual

cycle, but are much closer to measurements in winter than in summer, indicating unaccounted emissions in Chongqing and the greater area north of JGJ in the prior emission estimate.
Similar to JGJ, the GSN station (fig. 13) in the south of South Korea is influenced by East Asian emissions, but is situated further away from large sources. Therefore, measured mixing ratios are generally much lower and peaks are less pronounced, rarely reaching above 6 ppt. As the measurement error is mostly at the constant value of 0.1 ppt, posterior mixing ratios capture measured ones very well and are higher than a priori, indicating underestimated emissions. Every summer during June to September, both observed and modelled mixing ratios exhibit local minima, capturing the East Asian summer monsoon which transports less polluted air from the SH to GSN, an effect analysed in detail by Li et al. (2018). The drawdown of modelled mixing ratios is a combination of a lower baseline, mainly consisting of SH airmasses, and less influence from emission during 100 d prior to sampling, as airmasses arrive from the ocean instead of East Asian landmasses.

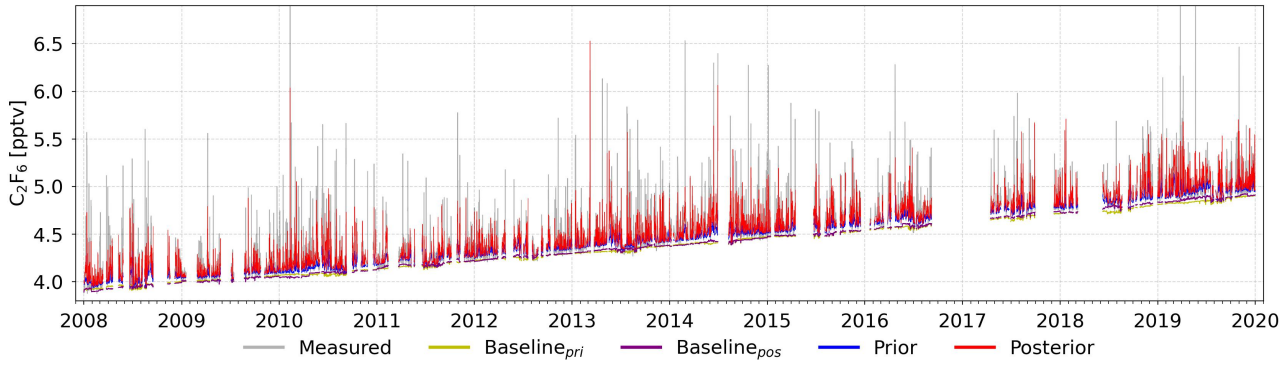

Fig. 13 GSN: Mixing ratio time series at the Gosan measurement station. The grey line shows measured mixing ratios. The yellow and purple lines represent prior and posterior baselines. Blue and red lines illustrate prior and posterior modelled mixing ratios. Minima in summer are introduced by the East Asian summer monsoon, transporting SH airmasses to Gosan.

Contrary to the previous two stations, measurements at MHD are much more representative of NH background mixing ratios and generally less influenced by emissions during 100 d prior to sampling. The reason is the seasonally independent prevailing westerly winds transporting well-mixed air masses from the northern Atlantic Ocean to MHD. Only occasionally, more polluted air from continental Europe reaches the station, producing individual mixing ratio peaks shown in fig. 14. Interestingly, measured peaks are more frequent and more pronounced until the early 2010s, compared to more recent years, indicating lower emissions in regions constrained by MHD measurements, as transport patterns did not change significantly. Say et al. (2021) identified a large emission decrease in Ireland until 2010 due to the replacement of C_2F_6 with NF_3 by an electronics manufacturer near Dublin, further strengthening this hypothesis. However, although

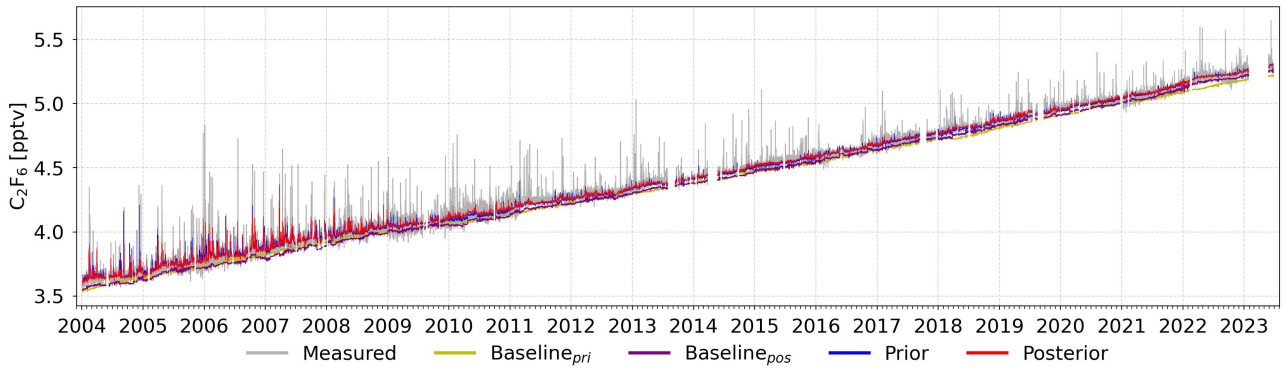

Fig. 14 MHD: Mixing ratio time series at the Mace Head measurement station. The grey line shows measured mixing ratios. The yellow and purple lines represent prior and posterior baselines. Blue and red lines illustrate prior and posterior modelled mixing ratios. Peak values correspond to pollution events transporting airmasses from the East to Mace Head

the peaks are lower in recent years, modelled posterior mixing ratios do not capture these at all, possibly indicating a missing emission source in the prior estimate which the model is not able to correct.

Another feature more apparent at background stations is the influence of the baseline optimisation. In general, the posterior baseline does not deviate much from the prior baseline, confirming the good performance of the FLEXPART-LCM global reanalysis simulations, from which the baseline is constructed. Only from 2022 onwards, the baseline optimisation produces a particularly strong deviation from the prior, with increments equivalent to emissions of several months (approx. 0.05 ppt). However, this is likely an artifact stemming from the small number of individual measurement stations from 2022 onwards (see sec. 3.2).

5.2. National and regional emission estimates

In the following section, time series of national or regional emissions for the study period are presented, analysed and compared to other BU and TD inventories when available. The EDGAR estimate is not shown directly for some regions, where a priori emissions were directly taken from EDGAR without any adjustment, therefore the prior equals EDGAR emissions. Gridded data from EDGAR or FLEXINVERT+ was integrated for each region depending on the area of a grid cell's intersection with the region's territory. The uncertainties of each region were estimated using Gaussian error-propagation including cross-correlations between different cells. For all regions, FLEXINVERT+ results with applied non-negativity constraint, and results with both the total global and non-negativity constraint applied, are presented to analyse the impact of the total global constraint method in different scenarios.

Asia

Emissions in China are presented in fig. 15 and represent the largest fraction of global emissions. Fortunately, a large number of measurements and individual stations constrain Chinese emissions well, particularly in 2011, 2012 and between 2016 to 2021, as indicated by the large uncertainty reduction. In 2004-2006 and 2022-2023, no East Asian measurements are available, resulting in nearly no increment or uncertainty reduction. For this reason, FLEXINVERT+ results are not interpreted for these years in China. However, applying the total global constraint to FLEXINVERT+ results, significantly increases Chinese emissions in 2022-2023 to close the global gap towards the box model estimate, indicating that emissions are otherwise underestimated in China. A similar absolute increase stemming from the total global constraint is not observed in 2004-2006, as globally fewer observations are available during this period, and uncertainties are also large in other regions such as Japan or Europe. When comparing emissions during this period to subsequent years, the constrained emissions likely do not capture true emissions as aluminium and electronics industries did not experience such large growth between 2006 and 2007.

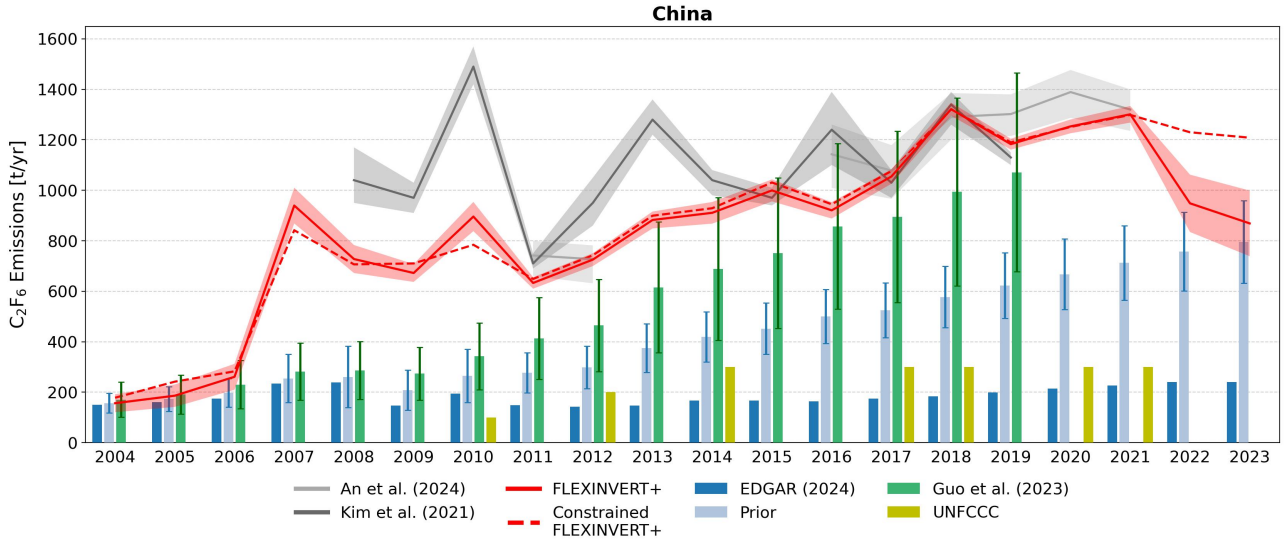

Fig. 15 Annual BU (bars) and TD (lines) emissions in China between 2004 and 2023. Non-negative constrained (solid red) and both non-negative and total global constrained (dashed red) FLEXINVERT+ results are presented with results by An et al. (2024) (light grey) and Kim et al. (2021) (dark grey). BU inventories include EDGAR (2023), Guo et al. (2023), UNFCCC (2024b) and a combination of the first two, used as the prior emissions in the inversion. The uncertainty of the prior is assigned as 100% of the emission magnitude per grid cell.

During the 2007-2011 period, Chinese emissions were at $738 \pm 60\,\mathrm{t/yr}$ and increased to $1227 \pm 48\,\mathrm{t/yr}$ within the 2017-2021 period, amounting to a relative increase of $66 \pm 12\,\%$ between these periods (Note that uncertainties are relatively small due to formal error propagation

and likely too small prior uncertainties). FLEXINVERT+ results agree reasonably well with estimates from Kim et al. (2021), who only used measurements from GSN for their inversion setup, but their results exhibit higher year-to-year variability. Due to the industrial nature of C_2F_6 sources, such large variations are likely an artefact of low observational constraints by only one station, primarily in western China. Another regional TD study by An et al. (2024) recently published inversion results only using measurements of the CMA network with higher spatial coverage over China. However, the number of individual measurements is sparse from 2013 to 2015, where their inverse modelling results are therefore not published. When results by An et al. (2024) are available, agreement with FLEXINVERT+ estimates is generally very good, capturing a similar trend of rising emissions. Due to the inclusion of measurements at GSN additionally to all Chinese stations' observations, FLEXINVERT+ results are still robust in 2013-2015, not exhibiting large year-to-year variability, although the uncertainty reduction decreases during this period. While both the EDGAR and UNFCCC inventories are too low by a factor of 3 to 6, a BU inventory recently published by Guo et al. (2023) is close to TD estimates, particularly in the later half of the 2010s. From 2007 to the early 2010s, results from FLEXINVERT+ and Kim et al. (2021) demonstrate a large discrepancy to all BU estimates in China.

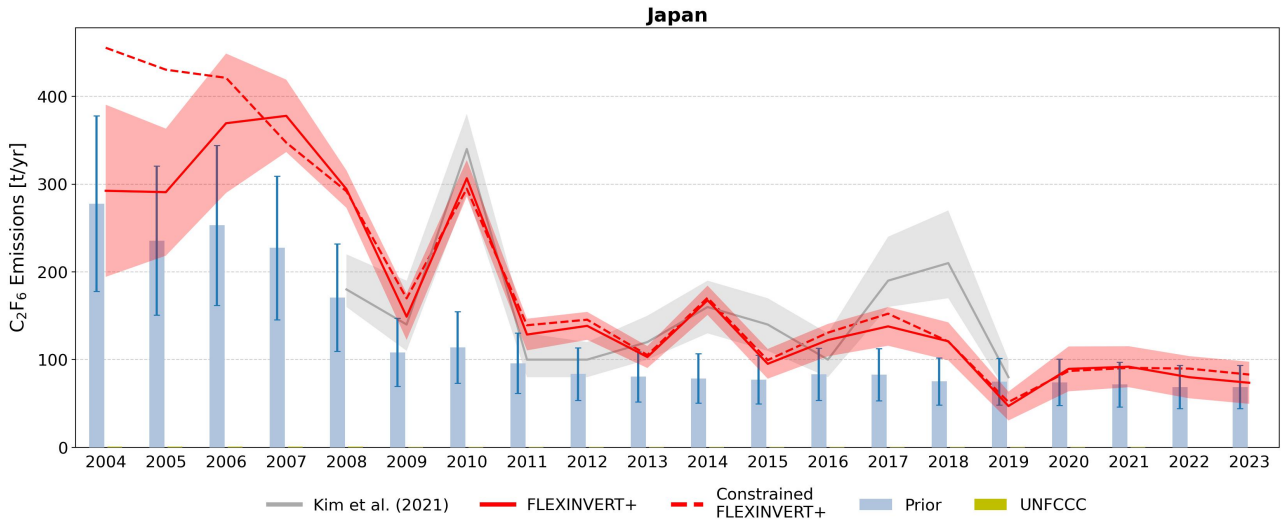

Fig. 16 Annual BU (bars) and TD (lines) emissions in Japan between 2004 and 2023. Non-negative constrained (solid red) and both non-negative and total global constrained (dashed red) FLEXINVERT+ results are presented with results by Kim et al. (2021) (dark grey). BU inventories include UNFCCC (2024a) and EDGAR (2023), which is directly used as the prior emissions in the inversion. The uncertainty of the prior is assigned as 100% of the emission magnitude per grid cell. UNFCCC emissions are close to zero and therefore barely visible.

Japanese C_2F_6 emissions decreased over the last two decades from 251 ± 51 t/yr in 2007-2011

to a relatively stable value of 97 ± 26 t/yr in 2017-2021, equivalent to a decrease in emissions of 61 ± 26 % between these time periods (fig. 16). Before 2008, when the posterior error is large due to missing observational constraint, the total global constraint increases emissions significantly and indicates a large discrepancy between TD and BU estimates, however the validity remains highly uncertain. The local maximum in 2010 is hypothesised by Kim et al. (2021), who found the same feature, to represent an overestimation of true emissions instead of a real signal, resulting from measurements at GSN and the atmospheric transport that affects this station. However, the local maximum in 2010, while not as high as resulting from FLEXINVERT+, might be correct to some extent. When looking at the signal in terms of a local minimum in 2009, which possibly results from decreased semiconductor manufacturing activity during the global financial crisis (GFC), the peak in 2010 is rather a continuation of pre-GFC emissions, following the general downward trend. The Tōhoku earthquake and tsunami could have possibly played a further role in reducing emissions in 2011, as electronics manufacturing factories had likely been destroyed. Results by Kim et al. (2021) agree very well with FLEXINVERT+ results with only minor differences likely resulting from differing model setups and the inclusion of Chinese measurements in this study, as they utilised the same transport and inversion models but only measurements at GSN. The discrepancy to the EDGAR inventory is also relatively small in most years, although the BU data exhibits a far smaller year-to-year variability compared to FLEXINVERT+ results. Japan's UNFCCC reports suggest emissions below 1t/yr (barely visible in fig. 16) for all years during the study period, which seems to be a strong underestimation of true emissions.

India has surpassed Russia and recently became the second largest producer of primary aluminium and is therefore likely a major contributor to global C_2F_6 emissions with rising importance. According to a recent study by Tan et al. (2025) on primary aluminium production, smelters in India rank among the most inefficient regarding the amount of CO_2-equivalent GHGs emitted per unit of produced aluminium, although not differentiating between electricity-related and process-related emissions. Tan et al. (2025) also predict a further increase of process-related PFC emissions in India, even under the best-case scenario. It is therefore crucial to estimate emissions using measurement-based TD methods and identify potential discrepancies to BU inventories.

FLEXINVERT+ results suggest relatively stable emissions between 2007 and 2016, averaging 78 ± 40 t/yr and a strong increase in 2017 reaching mean emissions of 261 ± 66 t/yr between 2017 and 2021; an increase of 233 ± 154 % (fig. 17). However, when interpreting results, it has to be noted that emissions in India are poorly constrained compared to other high-emission regions due to generally large distances to measurement stations and unfavourable prevailing circulation patterns. In fig. 17, the effect of the poor constraint is evident, as uncertainty reductions are very small for all years and emission increments are low, particularly

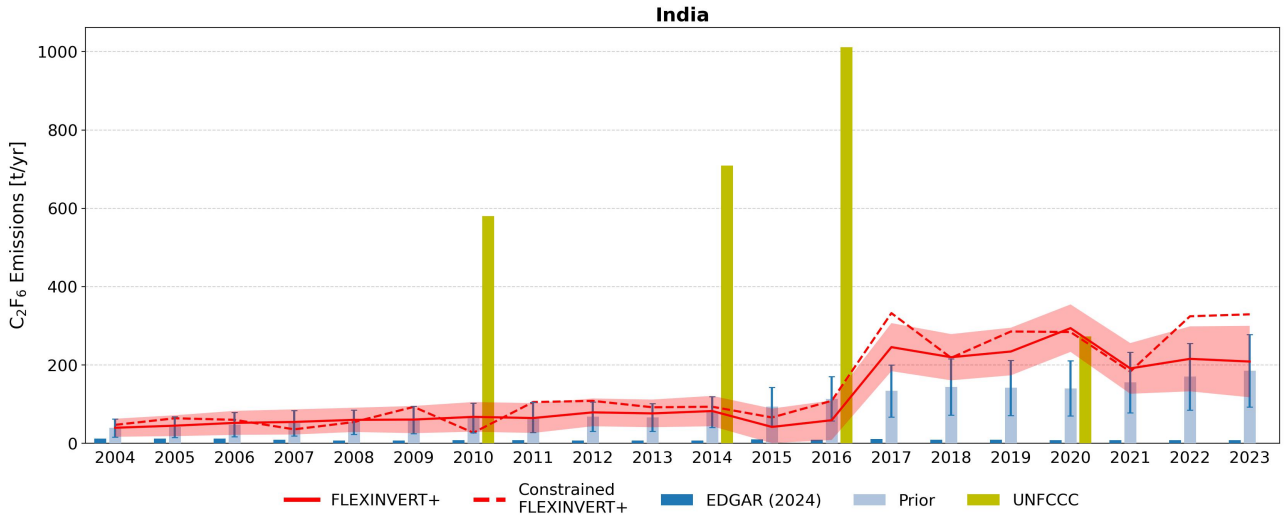

Fig. 17 Annual BU (bars) and TD (lines) emissions in India between 2004 and 2023. Non-negative constrained (solid red) and both non-negative and total global constrained (dashed red) FLEXINVERT+ results are presented. BU inventories include EDGAR (2023), UNFCCC (2024b) and a combination of the 2020 UNFCCC value and EDGAR, used as the prior emissions in the inversion. The uncertainty of the prior is assigned as 100% of the emission magnitude per grid cell.

before 2015. While FLEXINVERT+ results seem relatively stable between different years, tests suggested a strong dependency of posterior emissions on a priori emission magnitudes. The large discrepancy between the only two available BU inventories, EDGAR and India's reports to the UNFCCC, make further assessment of the inversion results' accuracy difficult. When comparing C_2F_6 emission magnitudes to those of Russia or Canada, which produce similar amounts of aluminium, EDGAR data is too low and UNFCCC values are too high, particularly those in 2010, 2014, and 2016. Only the estimate for 2020 from India's latest UNFCCC report agrees well with that year's inversion result, but the agreement is highly uncertain. It is therefore crucial to establish C_2F_6 measurements in India to enable more robust TD inverse modelling estimates.

Other significant emission regions in Asia include South Korea, Taiwan, Malaysia+Singapore and Russia, with averaged emissions of 79 ± 15 t/yr, 76 ± 23 t/yr, 165 ± 57 t/yr, 106 ± 29 t/yr between 2007 and 2021, respectively. Further detail on these regions are either given in sec. 5.3 or beyond the scope of this work.

Europe

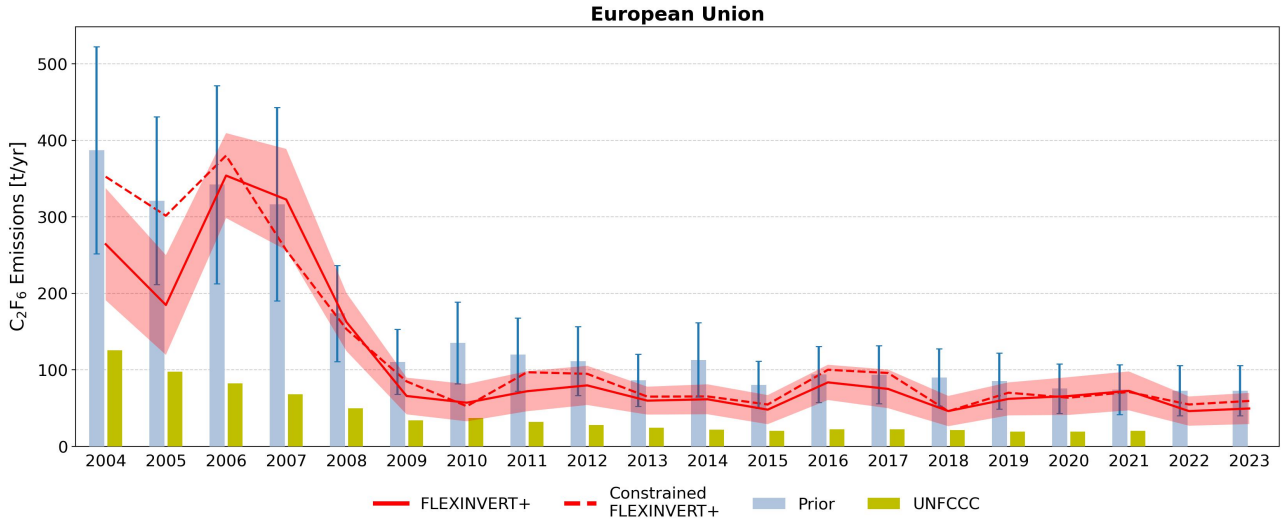

Fig. 18 Annual BU (bars) and TD (lines) emissions in all 27 European Union countries between 2004 and 2023. Non-negative constrained (solid red) and both non-negative and total global constrained (dashed red) FLEXINVERT+ results are presented. BU inventories include UNFCCC (2024a) and EDGAR (2023), which is directly used as the prior emissions in the inversion. The uncertainty of the prior is assigned as 100% of the emission magnitude per grid cell.

Emissions of all current 27 EU countries combined are presented in fig. 18, highlighting a strong decrease of C_2F_6 emissions during the second half of the 2000s and relatively stable emissions from 2009 onwards at $63 \pm 22\,\mathrm{t/y}$. The inversion achieves a reasonable uncertainty reduction, indicating good observational coverage and robustness of FLEXINVERT+ results. However, there is a significant difference between well observed western Europe and less constrained eastern Europe, as shown in the examples of Romania and Germany below.

In general, the agreement between FLEXINVERT+ results and EDGAR emissions is high, while the emissions reported to the UNFCCC by the EU likely underestimate the real magnitude. The largest differences between the EDGAR estimate and the unconstrained posterior emissions occur in 2004 and 2005 when observational coverage is minimal, however, the constrained posterior emissions agree well with EDGAR, indicating that the lower values are likely a result of the small number of measurements instead of a true signal. Many EU countries exhibit decreasing emissions in the late 2000s due to efforts in replacing C_2F_6 or implementing abatement techniques by European semiconductor manufacturers (ESIA, 2001), technological improvements leading to fewer AEs during aluminium smelting and the general decrease in aluminium and semiconductor production following the global financial crisis. For instance, when comparing inversion results from the 2004-2008 with the 2009-2023 period, Ireland's emissions decreased by $95 \pm 22\,\%$ and France's by $81 \pm 27\,\%$, making the contribution by most European

countries to the total global emissions small in recent years. Furthermore FLEXINVERT+ results agree well with results published by Say et al. (2021) for the Benelux region, France, Germany, Ireland and the United Kingdom, who used the same measurement dataset but different transport and inversion models.

Romania is the largest contributor to EU's and Europe's total emissions, particularly in the 2000s and the second half of the 2010s. For instance, when averaged over 2016-2021, Romania's contribution amounts to $44 \pm 31\,\%$ of EU emissions. While observational constraint is rather limited, the inversion increment is relatively large, as the prior emissions and therefore uncertainty is larger than in most other regions in Europe, giving the inversion more freedom for optimisation. Emissions in Romania, similar to most European countries, drastically decreased in the late 2000s by $73 \pm 31\,\%$ from the 2004-2008 to the 2009-2013 period. The largest emitter is believed to be a single aluminium smelter in Slatina, the production of which only dropped by 5.4 % during the same time according to British Geological Survey (2025). This leads to the hypothesis, that the emission decrease results from the implementation of measures to reduce AEs. In 2020, the company itself claims to have reduced its PFC emissions by 98% compared to 2002 (ALRO, 2020). FLEXINVERT+ estimates and EDGAR emissions are generally within the error range, however UNFCCC data likely underestimate real emissions by a large amount.

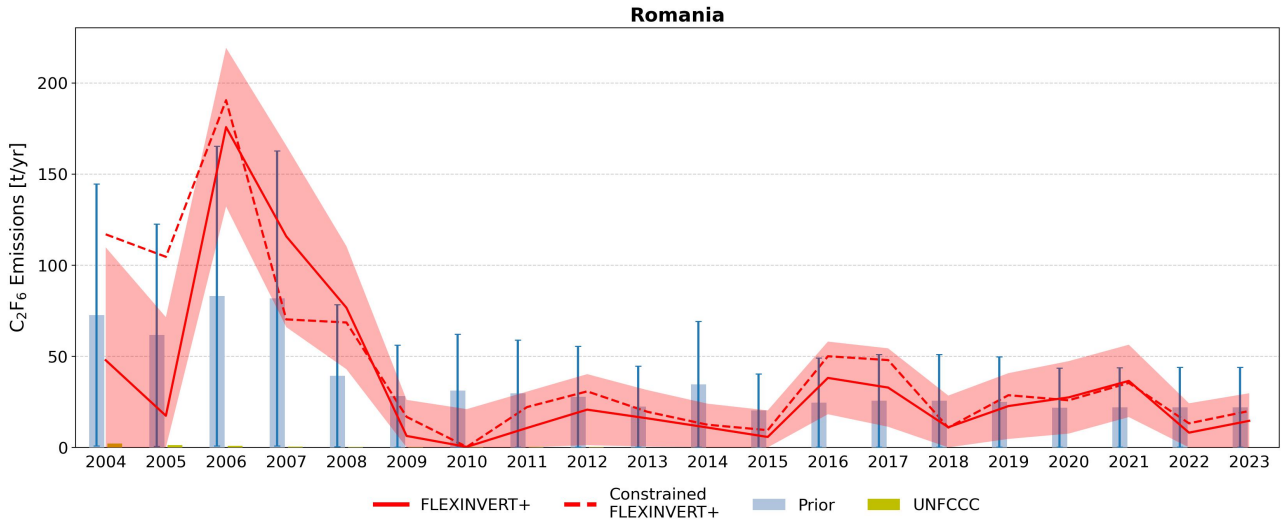

Fig. 19 Annual BU (bars) and TD (lines) emissions in Romania between 2004 and 2023. Non-negative constrained (solid red) and both non-negative and total global constrained (dashed red) FLEXINVERT+ results are presented. BU inventories include UNFCCC (2024a) and EDGAR (2023), which is directly used as the prior emissions in the inversion. The uncertainty of the prior is assigned as 100% of the emission magnitude per grid cell. UNFCCC emissions are close to zero and therefore barely visible.

Germany's C_2F_6 emissions are among the highest in western Europe, yet remain below 20 t/yr from 2008 onwards (fig. 20). Averaged over 2004-2007, EDGAR estimates emissions of 71 t/yr

and Germany's UNFCCC reports states 16 t/yr while the FLEXINVERT+ results suggest 39 ± 16 t/yr. From 2008 onwards, FLEXINVERT+ results still lie in between EDGAR and UNFCCC emissions, but agree better with both inventories due to the generally lower magnitudes. Say et al. (2021) performed a C_2F_6 inverse modelling study for western Europe, including Germany, which is in excellent agreement with FLEXINVERT+ results, confirming the reliability of the results. Germany is among the best constrained regions worldwide, resulting in a large reduction of uncertainty during the whole study period and leading to no significant impact of the total global constraint method, which mostly offers an additional constraint in less observed regions. These results further motivate the need for more observation stations at high sampling rates in currently less constrained regions to achieve similarly robust results as in Germany.

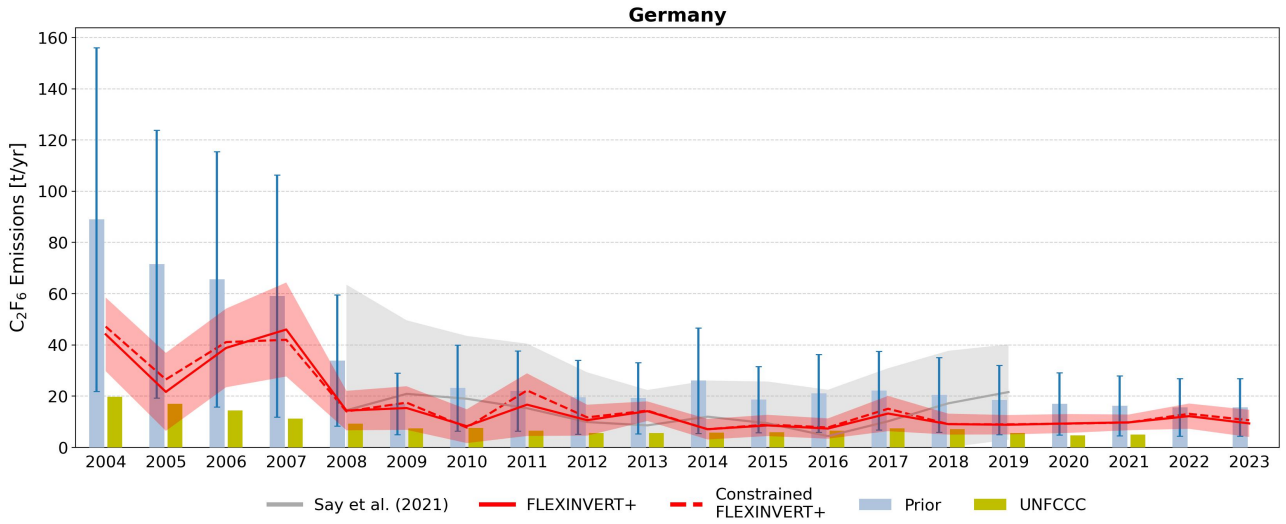

Fig. 20 Annual BU (bars) and TD (lines) emissions in Germany between 2004 and 2023. Non-negative constrained (solid red) and both non-negative and total global constrained (dashed red) FLEXINVERT+ results are presented with results by Say et al. (2021) (light grey). BU inventories include UNFCCC (2024a) and EDGAR (2023), which is directly used as the prior emissions in the inversion. The uncertainty of the prior is assigned as 100% of the emission magnitude per grid cell.

North America

While there have been regional TD studies estimating emissions in Europe and East Asia, this study presents the first TD emission estimate for C_2F_6 in North America, primarily USA and Canada, as emissions in Mexico are small. USA and Canada are both countries with high observational constraint from measurements in the USA and even Europe, due to the long backward simulation period, leading to relatively large error reductions.

FLEXINVERT+ results in the US agree well with both the EDGAR and UNFCCC estimate during the whole study period (fig. 21). The relatively large error reduction in most years

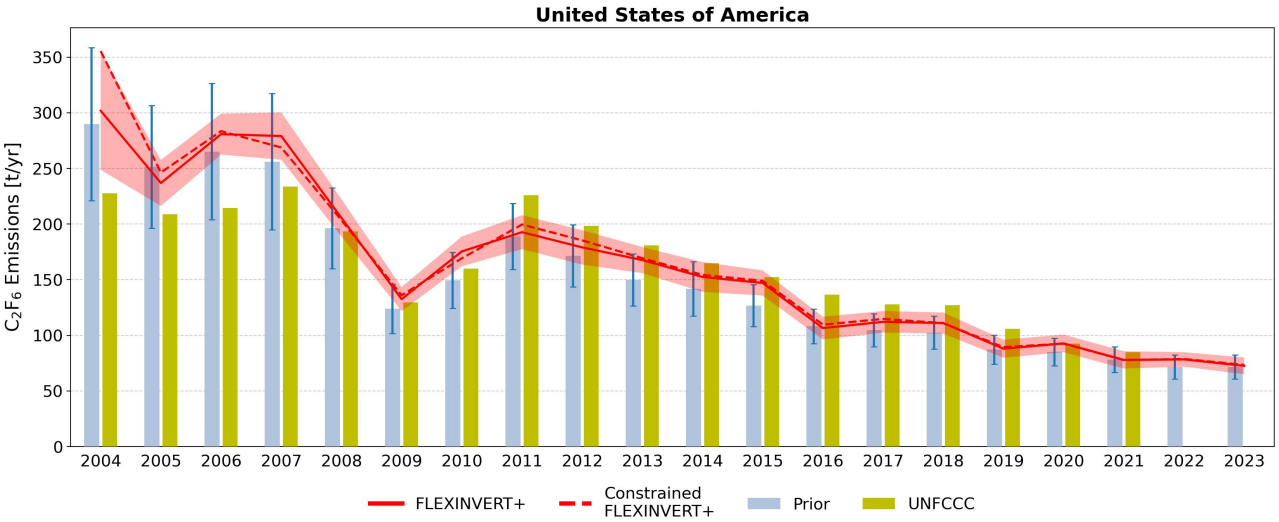

Fig. 21 Annual BU (bars) and TD (lines) emissions in the US between 2004 and 2023. Non-negative constrained (solid red) and both non-negative and total global constrained (dashed red) FLEXINVERT+ results are presented. BU inventories include UNFCCC (2024a) and EDGAR (2023), which is directly used as the prior emissions in the inversion. The uncertainty of the prior is assigned as 100% of the emission magnitude per grid cell.

suggests that the agreement comes from accurate BU inventories instead of small increments due to low observational constraints. Average emissions amount to 163 ± 24 t/yr over the whole period and decrease steadily. However, there is a clear local minimum around 2009, which is the strongest signal of the global financial crisis observed, among all regions. While the semiconductor and electronics industry demonstrated relatively good resilience, the aluminium industry experienced a strong decline in demand during that period leading to lower production and therefore lower C_2F_6 emissions (Board of Governors of the Federal Reserve System (US), 2025a, 2025b). This suggests that, at least around 2009, USA's emissions were still strongly driven by the aluminium industry, however a quantitative value on the fraction of emissions per industry is difficult to determine.

Canada exhibits large emissions in the EDGAR dataset throughout the study period, peaking in 2007 and declining ever since, but constantly remaining above 50 t/yr. In contrast, Canada's own estimate, contained in the UNFCCC emission dataset, lies at 7%-20% of EDGAR's between 2006 and 2021. Particularly European measurements constrain Canada's emissions well, which are believed to mainly occur on the East coast in Quebec at aluminium smelters located in that region (Sept-Îles, Alma, Bécancour). The long back trajectories of 100 d likely also contribute to higher sensitivities of European observation stations to Canada's emissions, leading to large relative error reductions. Apart from local peaks in 2004 and 2014-2015, FLEXINVERT+ posterior emissions agree far better with UNFCCC data than the EDGAR estimate which was used as a priori emissions in the inversion. Although there is no certain way to confirm the

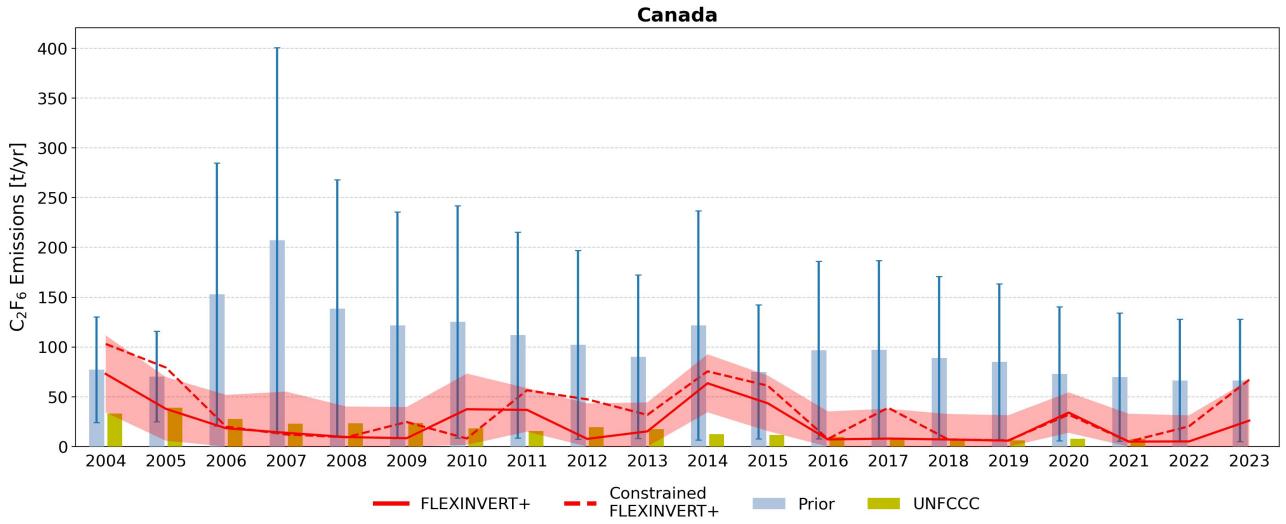

Fig. 22 Annual BU (bars) and TD (lines) emissions in the Canada between 2004 and 2023. Non-negative constrained (solid red) and both non-negative and total global constrained (dashed red) FLEXINVERT+ results are presented. BU inventories include UNFCCC (2024a) and EDGAR (2023), which is directly used as the prior emissions in the inversion. The uncertainty of the prior is assigned as 100% of the emission magnitude per grid cell.

accuracy of the inversion results, UNFCCC data suggest that the large negative increment the model produces is somewhat realistic. An analysis by Tan et al. (2025) also suggests that CO_2-equivalent GHG emission factors of Canada's aluminium smelters are among the lowest in the world, although they only present total GHG factors, which take electricity production into account, instead of C_2F_6 or PFC specific ones.

5.3. Global emission estimates and country contributions

In the following chapter, FLEXINVERT+ results of total global C_2F_6 emissions are presented and compared to other global emission inventories. The leading countries responsible for total emissions and emission trends are identified and their impact is quantified. A reassessment of the BU to TD discrepancy is presented and analysed for key countries. Lastly, further analysis on the impact of the novel total global constraint method is shown in this section.

Global emissions and trends

Fig. 23 shows a time series of global emissions from different BU and TD inventories as well as this study's FLEXINVERT+ results with 1) only the non-negativity constraint applied and 2) both the non-negativity and the total global constraint applied. Emissions between 2007-2011 amount to 2.17 ± 0.25 kt/yr on average, then drop to 1.81 ± 0.10 kt/yr for 2012-2016 and are restored back to 2.18 ± 0.11 kt/yr during the most recent period from 2017-2021. The difference between the second and third period represents a 20 ± 9 % increase of C_2F_6 emissions.

FLEXINVERT+ results are generally in good agreement with the two other global TD emission estimates by Say et al. (2021) and Rigby et al. (2014), particularly from 2008 to 2021, when most measurements are available. The uncertainty of FLEXINVERT+ is likely underestimated, as the inter-annual variability is much larger compared to its uncertainty magnitude and such large year-to-year variations are assumed unrealistic for C_2F_6. Only the signal in 2009 could be explained by lower global industrial activity following the GFC. Kim et al. (2021) also reported large year-to-year variations in their C_2F_6 inversion results and suspected the reason to stem from measurements at the GSN station. The variability from 2011 onwards is much lower, as the inclusion of Chinese measurements, starting in 2011, and the subsequently higher constraint on East Asian emissions might lead to more robust results, further strengthening the hypothesis by Kim et al. (2021).

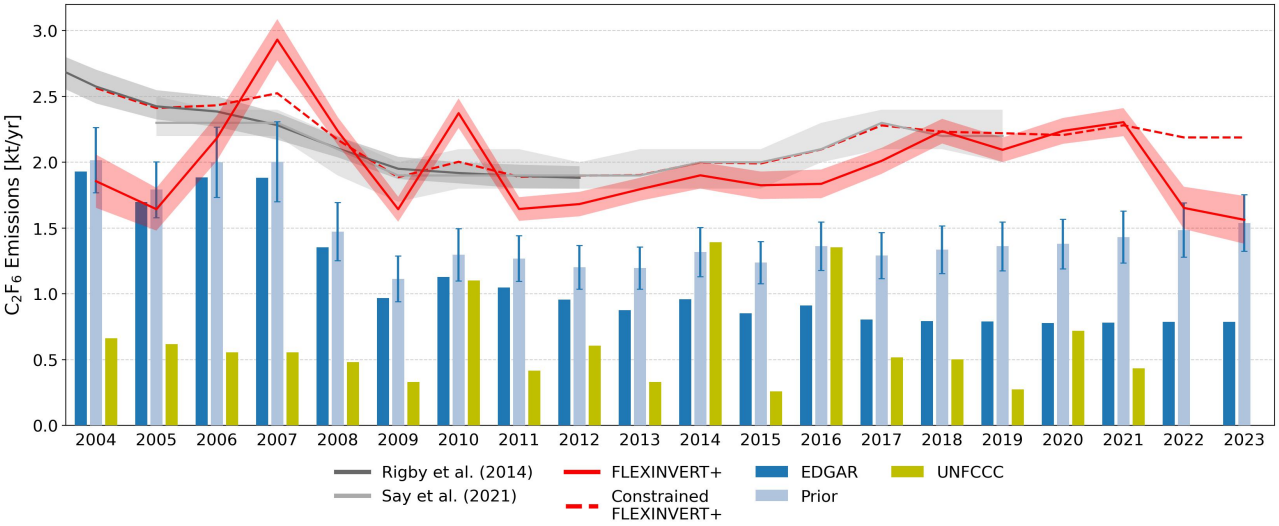

Fig. 23 Annual total global BU (bars) and TD (lines) emissions between 2004 and 2023. Non-negative constrained (solid red) and both non-negative and total global constrained (dashed red) FLEXINVERT+ results are presented with results from the AGAGE 12-box model by Say et al. (2021) (light grey) and Rigby et al. (2014) (dark grey). BU inventories include UNFCCC (2024a), EDGAR (2023), and a combination of BU inventories which is used as the prior emissions in the inversion. The uncertainty of the prior is assigned as 100% of the emission magnitude per grid cell.

Due to the small number of individual measurement stations in 2004-2006 and 2022-2023, the posterior emissions and uncertainties do not deviate much from their prior counterparts. However, constraining the inversion results towards the box model estimates removes both the underestimation at the start and end of the study period as well as the large variability in the 2000s and yields values close to the box model, as intended. Comparing the TD results to EDGAR's BU inventory displays a large discrepancy, smaller at the beginning of the study period and larger towards the end at a factor of up to 3, due to the steady decrease of BU

estimates, while TD emissions increase from 2011 onwards. The UNFCCC data exhibits more variability due to the limited number of reports by a few key countries, such as the likely overestimation of India's emissions in their 2010, 2014 and 2016 reports. While the self-constructed, BU-based a priori estimate is higher than the other BU inventories in most years, it is still lower than TD results. This large discrepancy again confirms that there are unaccounted emissions in BU inventories.

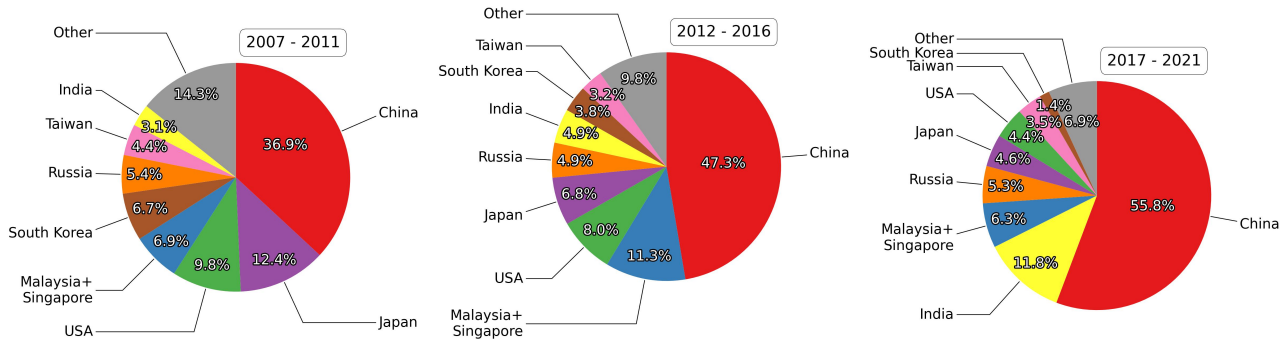

$2.17 \pm 0.25\,\mathrm{kt/yr}$ $1.81 \pm 0.10\,\mathrm{kt/yr}$ $2.18 \pm 0.11\,\mathrm{kt/yr}$

Fig. 24 Pie diagrams illustrating the fraction of each region's emissions to global C_2F_6 emissions (bottom), averaged over 2007-2011, 2012-2016, and 2017-2021. China contributed most to global emissions in all periods and exhibits an increasing trend.

The three pie diagrams in fig. 24 show the fraction of global emissions per country, with the total global constraint applied, averaged over 5 year intervals between 2007 and 2021 and illustrate the shifting emission pattern among major contributing countries. China has the largest emission share during the whole period, increasing from $36.9 \pm 5.3\,\%$ in 2007-2011 to $55.8 \pm 3.7\,\%$ in 2017-2021. The second, third and fifth largest emitters during 2007-2011, Japan, USA, and South Korea, significantly reduced their shares of global emissions from $28.9 \pm 3.4\,\%$ to $10.4 \pm 1.4\,\%$ in 2017-2021. Particularly Japan and South Korea facilitate large electronics industries with nearly no primary aluminium production, indicating successful strategies in mitigating C_2F_6 emissions through abatement and replacement with alternative etching gases. The Taiwan region, Russia, Malaysia and Singapore experience no significant change of their global emission shares, either due to strong growth of the respective industries offsetting decreasing emissions through mitigation strategies or no mitigation efforts while industry activity remains constant. However, emissions in these regions are highly uncertain, particularly in Malaysia and Singapore due to missing observational constraint. India exhibits the largest relative growth of it's global emission share rising from $3.1 \pm 1.6\,\%$ in 2007-2011 to $11.8 \pm 3.0\,\%$ in 2017-2021 due to the strong growth of its aluminium industry (British Geological Survey, 2025), but inversion results in India remain highly uncertain. The share of other, not individually shown, countries drops significantly from $14.3 \pm 4.2\,\%$ to $6.9 \pm 1.6\,\%$, mostly due to emission decreases in Europe, while global emissions remain constant or increase.

Fig. 25 shows the emission differences between the three periods presented above (2007-2011, 2012-2016, 2017-2021) per contributing country and the net global trend. Looking at the net global trend, there is no significant emission difference between the first and third period, while the trend is negative from the first to the second and positive from the second to the third period. Emission differences in individual regions differ strongly depending on the investigated period. China is the largest contributor to the global emission growth with a total increase of 449 ± 91 t/yr between 2007-2011 and 2017-2021. India's emission increase represents the second largest, which almost exclusively occurred between the 2012-2016 and 2017-2021 periods and in total amounts to a difference of 198 ± 76 t/yr between the third and first period. In most other countries, emission reductions were achieved, primarily in Japan, South Korea, USA, and most EU countries among others. However, the highest reductions occur between period 1 and 2 where they could more than offset the positive trend in China and some other regions. The magnitude of emission reductions declined in most regions between the second and third period compared to the reductions from the first to second period, indicating that mitigation efforts had stalled during the 2010s or at least did not achieve large emission reductions in absolute terms. On the contrary, the opposite effect is observed for regions with increasing emission trends, primarily China and India, where the emission increase is larger in recent years. This results in the emission increase in China and India not being offset by emission reductions in most other regions, leading to a net emission growth of 369 ± 151 t/yr between the 2012-2016 and 2017-2021 periods. Most notably, the Chinese emission growth alone is of similar magnitude as the global growth between these time periods, while India's relative growth of the emission trend is by far the largest.

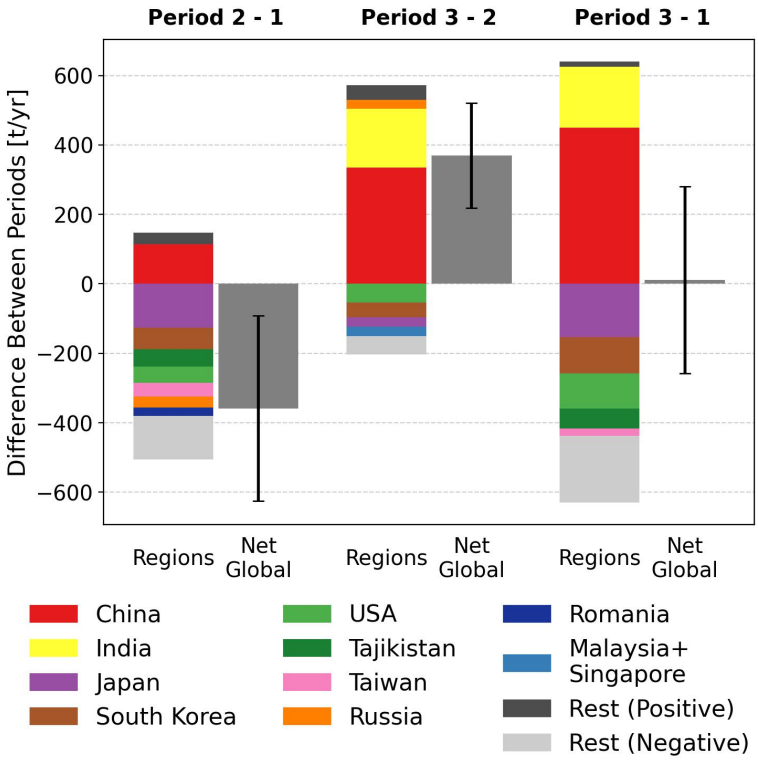

Fig. 25 Difference in emissions between three periods: 2007-2011 (1), 2012-2016 (2), 2017-2021 (3). Values for most relevant regions are presented by coloured bars on the left of each period difference and the grey bar on the right represents the net global difference. Emissions decreased between the first and second periods, but increased from the second to the third period, resulting in no significant trend overall.

TD to BU discrepancy reassessment

To reassess where the largest differences between TD and BU emission estimates of C_2F_6 lie, fig. 26 presents each region's contribution to the global discrepancy in percent, again for the three periods already used above. As the TD estimate, FLEXINVERT+ posterior constrained by the total global emissions is chosen and compared to the EDGAR BU inventory which provides the most temporally and regionally complete inventory. In the majority of regions, the discrepancy is positive, meaning that the TD method estimates higher emissions than the BU data. However, Canada exhibits a significant negative discrepancy of $-14 \pm 5\,\%$ during 2007-2011 among other minor regions with negative discrepancies, which reduces significantly in later years. On average between 2007 and 2021, China contributes $69 \pm 10\,\%$ to the global BU to TD discrepancy, making it by far the largest source of error in the EDGAR dataset in absolute numbers, assuming TD estimates are closer to reality. While between 2007 to 2011, South Korea's and Japan's contribution was also relatively large at $16 \pm 4\,\%$ and $13 \pm 6\,\%$, respectively, they shrunk to under 2% in the most recent period. BU emissions in India also underestimate the TD estimate at a rising rate with up to $17 \pm 5\,\%$ in 2017-2021. When interpreting these results, it is important to note that the uncertainties given with each contribution are only based on the posterior uncertainty from FLEXINVERT+, as the EDGAR dataset does not include an uncertainty assessment of its emissions. Therefore, the uncertainties are most likely underestimated.

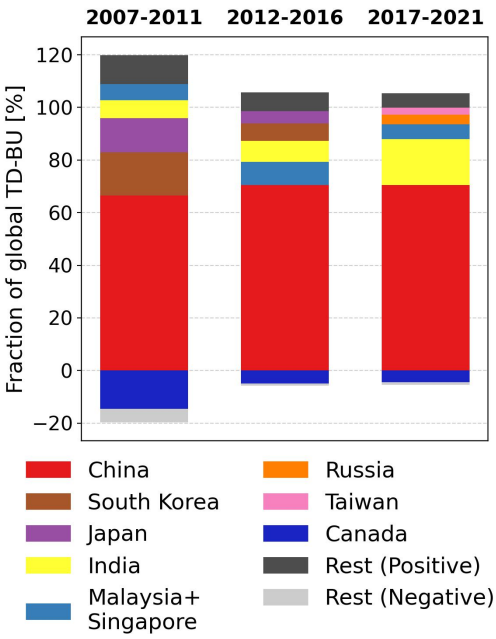

Fig. 26 Major emitting countries' contributions to the total discrepancy between FLEXINVERT+ (TD) and EDGAR (BU) emission estimates, averaged over three 5 y periods. Most countries exhibit higher TD than BU values, with China contributing most in all three periods.

Regional impact of total global constraint

To assess the impact of the newly developed total global constraint, not only on a global- and country-level but also regionally resolved, fig. 27 presents maps of the difference between the non-negativity constrained and both non-negativity and total global constrained FLEXINVERT+ results. In 2010, the method had a relatively large negative impact, as box-model results were overestimated by FLEXINVERT+. The largest impact is found at grid cells containing the highest emissions as these usually exhibit the highest posterior uncertainties as well. The total global constraint decreases emissions in most grid cells in 2010, yet regions neighbouring the East China Sea and in the north-west of the USA, demonstrate a positive impact.

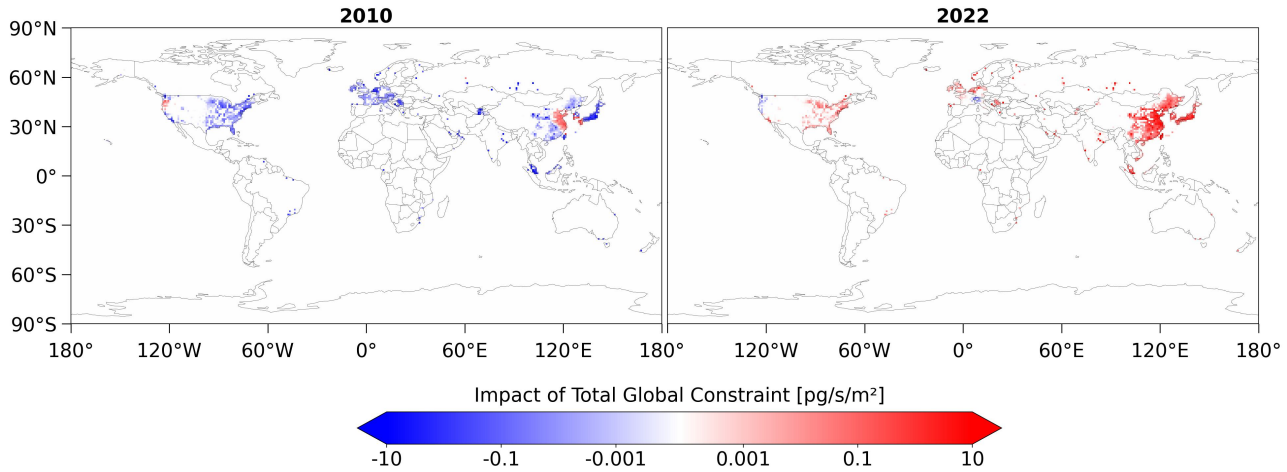

Fig. 27 Difference between FLEXINVERT+ results that were constrained both with the global total emissions and non-negativity of the emissions and results that were constrained only with non-negativity in 2010 and 2022. Red values indicate that the total global emission constraint leads to higher emissions, and vice versa for blue values. Highest impact occurs in grid cells with highest posterior uncertainty, corresponding to those with highest emissions.

The reason is likely negative correlations between these regions and other high-emission grid cells in the posterior error covariance matrix. Interestingly, the locations of the reversed impact correspond to regions highly constrained by the THD and GSN measurement stations, however no apparent difference of the measurements and atmospheric transport is found between these two and all other stations.

In 2022, the total global constraint method increases emissions in nearly all grid cells due to an underestimated global value by FLEXINVERT+ compared to the box model results. Again the largest impact is observed in regions with high emissions and uncertainties, mainly in Asia, Europe and North America. Negative correlations in East Asia have ceased, most likely as there is no measurement data from East Asia included in the inversion in 2022. In the grid cells around the THD station, negative correlations persist, now indicated by a negative impact of the total global constraint as the general direction of the optimisation is reversed. Additionally, regions covered by the JFJ station in Switzerland also seem to exhibit negative correlations in 2022.

6. Conclusion

This study presents the first regionally resolved global top-down (TD) emission estimate of hexafluoroethane (C_2F_6), one of the most potent and long-lived greenhouse gases GHG, known to be almost exclusively emitted by the aluminium and electronics industries. Measurements, averaged over 3 h intervals, at 32 observation stations worldwide, are combined with atmospheric

transport simulations and an a priori emission estimate compiled from several industry activity-based bottom-up (BU) inventories to infer a posteriori global emissions between 2004 and 2023. A source receptor relationship (SRR) for each measurement, relating potential source regions to the respective observation station, is constructed by simulating the atmospheric transport of virtual particles backward in time for 100 d. Prior to the backward simulation period, a background of C_2F_6 mixing ratios is obtained by combining the trajectory termination points with a custom global reanalysis of C_2F_6 obtained with FLEXPART-LCM, a recently improved model simulating emissions and transport of compounds in the atmosphere which utilises a simple nudging technique to constrain the model towards observed mixing ratios. The Bayesian inversion framework FLEXINVERT+ is utilized to combine the measurements, SRRs, background mixing ratios, and a priori emission estimates to yield the best estimate of a posteriori emissions and mixing ratios and model their uncertainties based on the errors of all components. A novel approach, constraining the total sum of a posteriori emissions towards well-known global emission values from a box model, is applied to counteract artefacts introduced by low observational constraints.

Results from the global C_2F_6 reanalysis with FLEXPART-LCM suggest a decent improvement over its predecessor FLEXPART-CTM in a validation run, excluding 10 measurement stations from nudging modelled fields. Activating nudging at measurement stations significantly improves the performance of the modelled fields, but caution needs to be taken when choosing appropriate kernel sizes. The reanalysis is able to capture complex transport patterns, such as the East Asian summer monsoon, affecting measurement stations in East Asia. However, the accuracy of modelled mixing ratio fields is strongly dependent on the magnitude and distribution of emissions, posing a problem for C_2F_6 as emissions are not well known.

Modelled a posteriori mixing ratios by FLEXINVERT+ agree well with measurements, particularly at background stations, and exhibit a large improvement from a priori values, as intended by the optimisation. Stations highly influenced by large or nearby emissions, mainly located in East Asia, exhibit the lowest performance metrics overall, but are crucial to constrain large fractions of global emissions. Modelled mixing ratios are able to represent special features, such as seasonally varying transport patterns or short emission events, as a combination of the baseline obtained with FLEXPART-LCM and explicitly modelled transport during the previous 100 d before measurement sampling by FLEXPART backward trajectories.

A posteriori global emissions (without the total global constraint) agree well with box model estimates published by Say et al. (2021) and Rigby et al. (2014) when the observational constraint, particularly in East Asia, is high (2011-2021). In the remaining years, either no significant increments from a priori emissions are apparent (2004-2006, 2022-2023), or unreasonably large year-to-year variability appears (2007-2010). Applying the total global constraint to box model values significantly reduces the difference to the relatively well-known box model emission

values, as intended, and distributes the added increments depending on a posteriori uncertainties across all regions. According to FLEXINVERT+ results, global emissions amounted to 2.17 ± 0.25 kt/yr, 1.81 ± 0.10 kt/yr, and 2.18 ± 0.11 kt/yr on average for the (1) 2007-2011, (2) 2012-2016, and (3) 2017-2021 periods, respectively.

China is by far the largest contributor to global C_2F_6 emissions at 36.9 ± 5.3 % in period 1 increasing to 55.8 ± 3.7 % in period 3. Emissions in China experience a strong increase, amounting to a difference of 449 ± 91 t/yr when comparing period 3 to period 1, approximately offsetting the decreasing emission trends of the 5 countries with the largest negative trends. FLEXINVERT+ results in China agree well with other regional TD studies, but are 3 to 6 times higher than the country's own reported emissions to the UNFCCC or the estimates by EDGAR (2023), both representing activity-based BU inventories. Only the BU emissions compiled by Guo et al. (2023) agree with TD values within error margins from 2013 to 2019. It is crucial to further develop BU approaches and identify the industries for which BU emissions underestimate the likely more realistic TD results.

Nearly all other economically developed regions, including EU countries, Japan, South Korea, Canada, and the US, have experienced large decreases in C_2F_6 emissions when comparing period 2 to period 1, likely through advancements in aluminium smelting technology and abatement implementations and substitutions with NF_3 by the electronics industry. However, between period 2 and period 3, emission reductions have decreased significantly in those regions, both in relative and absolute terms, indicating reduced mitigation efficiencies or efforts in the 2010s. Other regional TD estimates agree well with FLEXINVERT+ results, confirming a good performance of the proposed model setup. Comparisons to BU inventories yield mixed TD to BU discrepancies depending on the studied region (low in the USA, relatively high in the EU), highlighting the difficulty to achieve robust BU estimates with a limited number of observations.

India has established itself as a key C_2F_6 emitting region in recent years with a 11.8 ± 3.0 % share of global emissions in period 3 (261 ± 66 t/yr), almost exclusively as a result of its growing aluminium smelting industry. Tan et al. (2025) predict further growth for India's aluminium industry, while emission reduction measures are likely going to be implemented later than in most other regions. The available BU inventories (EDGAR, 2023; UNFCCC, 2024b) differ by a factor of up to 109 in 2016 and are therefore not reliable in India. In the future, it will be crucial to establish (or perhaps publish) C_2F_6 measurements in India to enable more accurate inverse modelling studies and revise emission factors specific to India's aluminium smelters for more accurate BU estimates.

Furthermore, little is known about C_2F_6 emissions in South America, Africa, and the Middle East region due to very small observational constraints and highly uncertain BU estimates. Atmospheric measurements and reliable reporting of industry data should be established in these regions to better constrain their emissions.

Methodological improvements in the inverse modelling approach could include a splitting of the observational dataset, where the highest measurements, most influenced by close-by emissions, are excluded from optimising the baseline during the inversion. This approach could reduce the variability of the optimised baseline while preserving a large influence of high measurements which likely include crucial information on emission events. Another limitation which should be addressed in further studies is the low posterior uncertainty of FLEXINVERT+ which does not account for systematic errors. Using an ensemble with different a priori emission distributions and magnitudes, and with randomly varying model parameters would most likely increase the posterior uncertainty, particularly in regions with low observational constraints (Vojta et al., 2025).

References

ALRO. (2020, June). News. Retrieved March 16, 2025, from https://www.alro.ro/en/investor-relations/news/alro-one-of-the-largest-vertically-integrated-aluminium-producers-in-europe-is-celebrating-its-55th-anniversary

An, M., Prinn, R. G., Western, L. M., Yao, B., Zhao, X., Kim, J., Mühle, J., Chi, W., Harth, C. M., Hu, J., Ganesan, A. L., & Rigby, M. (2024). Substantial increase in perfluorocarbons CF4 (PFC-14) and C2F6 (PFC-116) emissions in China. *Proceedings of the National Academy of Sciences*, *121*(30), e2400168121. https://doi.org/10.1073/pnas.2400168121

Bakels, L., Tatsii, D., Tipka, A., Thompson, R., Dütsch, M., Blaschek, M., Seibert, P., Baier, K., Bucci, S., Cassiani, M., Eckhardt, S., Groot Zwaaftink, C., Henne, S., Kaufmann, P., Lechner, V., Maurer, C., Mulder, M. D., Pisso, I., Plach, A., ... Stohl, A. (2024). FLEXPART version 11: Improved accuracy, efficiency, and flexibility. *Geoscientific Model Development*, *17*(21), 7595–7627. https://doi.org/10.5194/gmd-17-7595-2024

Bergamaschi, P., Segers, A., Brunner, D., Haussaire, J.-M., Henne, S., Ramonet, M., Arnold, T., Biermann, T., Chen, H., Conil, S., Delmotte, M., Forster, G., Frumau, A., Kubistin, D., Lan, X., Leuenberger, M., Lindauer, M., Lopez, M., Manca, G., ... Yver Kwok, C. (2022). High-resolution inverse modelling of European CH4 emissions using novel FLEXPART-COSMO TM5 4DVAR inverse modelling system. https://doi.org/10.5194/acp-2022-118

Beu, L. S. (2005, February). *Reduction of Perfluorocompound (PFC) Emissions: 2005 State-of-the-Technology Report* (tech. rep.). Austin, Texas. Retrieved November 17, 2024, from https://www.epa.gov/sites/default/files/2016-02/documents/final_tt_report.pdf

Board of Governors of the Federal Reserve System (US). (2025a, February). Industrial Production: Manufacturing: Durable Goods: Alumina and Aluminum Production and Processing. Retrieved March 16, 2025, from https://fred.stlouisfed.org/series/IPG3313A

Board of Governors of the Federal Reserve System (US). (2025b, February). Industrial Production: Manufacturing: Durable Goods: Semiconductor and Other Electronic Component. Retrieved March 16, 2025, from https://fred.stlouisfed.org/series/IPG3344S

British Geological Survey. (2025). World mineral statistics archive. Retrieved January 15, 2025, from https://www.bgs.ac.uk/mineralsuk/statistics/world-mineral-statistics/world-mineral-statistics-archive/

Cai, B., Liu, H., Kou, F., Yang, Y., Yao, B., Chen, X., Wong, D. S., Zhang, L., Li, J., Kuang, G., Chen, L., Zheng, J., Guan, D., & Shan, Y. (2018). Estimating perfluorocarbon emission factors for industrial rare earth metal electrolysis. *Resources, Conservation and Recycling*, *136*, 315–323. https://doi.org/10.1016/j.resconrec.2018.04.018

Calvo Buendia, E., Tanabe, K., Kranjc, A., Jamsranjav, B., Fukuda, M., Ngarize, S., Osako, A., Pyrozhenko, Y., Shermanau, P., & Federici, S. (2019). *2019 Refinement to the 2006*

IPCC Guidelines for National Greenhouse Gas Inventories. IPCC, Switzerland. https://www.ipcc-nggip.iges.or.jp/public/2019rf/index.html

Change, I. P. o. C. (1992, May). *Climate Change 1992*. Cambridge University Press.

Choi, J. (2023). Growth of the Chinese Semiconductor Industry. https://doi.org/10.58445/rars.252

Czerniak, M. (2018). PFC Emission Reduction in the Semiconductor Industry. In O. Martin (Ed.), *Light Metals 2018* (pp. 1495–1498). Springer International Publishing. https://doi.org/10.1007/978-3-319-72284-9_195

Dunse, B. L., Derek, N., Fraser, P. J., Krummel, P. B., & Steele, L. P. (2019). Australian and global HFC, PFC, Sulfur Hexafluoride, Nitrogen Trifluoride and Sulfuryl Fluoride Emissions 2019.

EDGAR. (2023). Emission Database for Global Atmospheric Research, release version 8, European Commission, Joint Research Centre (JRC), the International Energy Agency (IEA). Retrieved February 6, 2024, from http://edgar.jrc.ec.europa.eu

ESIA. (2001, December). *PFC Voluntary Agreement Report* (tech. rep.). Retrieved March 16, 2025, from https://www.eusemiconductors.eu/sites/default/files/uploads/20111214_ESIA_PerfluoroBrochure.pdf

Fabian, P., Borchers, R., Krüger, B. C., & Lal, S. (1987). CF4 and C2F6 in the atmosphere. *Journal of Geophysical Research: Atmospheres*, *92*(D8), 9831–9835. https://doi.org/10.1029/JD092iD08p09831

Fang, X., Saito, T., Park, S., Li, S., Yokouchi, Y., & Prinn, R. G. (2018). Performance of Back-Trajectory Statistical Methods and Inverse Modeling Method in Locating Emission Sources. *ACS Earth and Space Chemistry*, *2*(8), 843–851. https://doi.org/10.1021/acsearthspacechem.8b00062

Flerlage, H., Velders, G. J. M., & de Boer, J. (2021). A review of bottom-up and top-down emission estimates of hydrofluorocarbons (HFCs) in different parts of the world. *Chemosphere*, *283*, 131208. https://doi.org/10.1016/j.chemosphere.2021.131208

Groot Zwaaftink, C. D., Henne, S., Thompson, R. L., Dlugokencky, E. J., Machida, T., Paris, J.-D., Sasakawa, M., Segers, A., Sweeney, C., & Stohl, A. (2018). Three-dimensional methane distribution simulated with FLEXPART 8-CTM-1.1 constrained with observation data. *Geoscientific Model Development*, *11*(11), 4469–4487. https://doi.org/10.5194/gmd-11-4469-2018

Guo, L., Yang, Y., Fraser, P. J., Velders, G. J. M., Liu, Z., Cui, D., Quan, J., Cai, Z., Yao, B., Hu, J., & Fang, X. (2023). Projected increases in emissions of high global warming potential fluorinated gases in China. *Communications Earth & Environment*, *4*(1), 1–9. https://doi.org/10.1038/s43247-023-00859-6

Henne, S., Brunner, D., Groot Zwaaftink, C., & Stohl, A. (2018, May). FLEXPART 8-CTM-1.1: Atmospheric Lagrangian Particle Dispersion Model for global tracer transport. https://doi.org/10.5281/zenodo.1249190

Henne, S., Brunner, D., Oney, B., Leuenberger, M., Eugster, W., Bamberger, I., Meinhardt, F., Steinbacher, M., & Emmenegger, L. (2016). Validation of the Swiss methane emission inventory by atmospheric observations and inverse modelling. *Atmospheric Chemistry and Physics*, *16*(6), 3683–3710. https://doi.org/10.5194/acp-16-3683-2016

Hersbach, H., Bell, B., Berrisford, P., Hirahara, S., Horányi, A., Muñoz-Sabater, J., Nicolas, J., Peubey, C., Radu, R., Schepers, D., Simmons, A., Soci, C., Abdalla, S., Abellan, X., Balsamo, G., Bechtold, P., Biavati, G., Bidlot, J., Bonavita, M., ... Thépaut, J.-N. (2020). The ERA5 global reanalysis. *Quarterly Journal of the Royal Meteorological Society*, *146*(730), 1999–2049. https://doi.org/10.1002/qj.3803

Hodnebrog, Ø., Aamaas, B., Fuglestvedt, J. S., Marston, G., Myhre, G., Nielsen, C. J., Sandstad, M., Shine, K. P., & Wallington, T. J. (2020). Updated Global Warming Potentials and Radiative Efficiencies of Halocarbons and Other Weak Atmospheric Absorbers. *Reviews of Geophysics*, *58*(3), e2019RG000691. https://doi.org/10.1029/2019RG000691

IAI. (2020, August). *2019 Anode Effect Survey Report* (tech. rep.). Retrieved November 12, 2024, from https://international-aluminium.org/resources/2019-anode-effect-survey-report/

IAI. (2021, January). Primary Aluminium Production. Retrieved November 15, 2024, from https://archive.international-aluminium.org/statistics/primary-aluminium-production/

Illuzzi, F., & Thewissen, H. (2010). Perfluorocompounds emission reduction by the semiconductor industry. *Journal of Integrative Environmental Sciences*, *7*(sup1), 201–210. https://doi.org/10.1080/19438151003621417

Indian Bureau of Mines. (2025). Indian Minerals Yearbook. Retrieved February 15, 2025, from https://ibm.gov.in/IBMPortal/pages/Indian_Minerals_Yearbook

IPCC. (2023). *Climate Change 2021 – The Physical Science Basis: Working Group I Contribution to the Sixth Assessment Report of the Intergovernmental Panel on Climate Change*. Cambridge University Press. https://doi.org/10.1017/9781009157896

Kabanikhin, S. I. (2008). Definitions and examples of inverse and ill-posed problems. *Journal of Inverse and Ill-posed Problems*, *16*(4), 317–357. https://doi.org/10.1515/JIIP.2008.019

Kim, J., Fraser, P. J., Li, S., Mühle, J., Ganesan, A. L., Krummel, P. B., Steele, L. P., Park, S., Kim, S.-K., Park, M.-K., Arnold, T., Harth, C. M., Salameh, P. K., Prinn, R. G., Weiss, R. F., & Kim, K.-R. (2014). Quantifying aluminum and semiconductor industry perfluorocarbon emissions from atmospheric measurements. *Geophysical Research Letters*, *41*(13), 4787–4794. https://doi.org/10.1002/2014GL059783

Kim, J., Thompson, R., Park, H., Bogle, S., Mühle, J., Park, M.-K., Kim, Y., Harth, C. M., Salameh, P. K., Schmidt, R., Ottinger, D., Park, S., & Weiss, R. F. (2021). Emissions of Tetrafluoromethane (CF4) and Hexafluoroethane (C2F6) From East Asia: 2008 to 2019. *Journal of Geophysical Research: Atmospheres*, *126*(16), e2021JD034888. https://doi.org/10.1029/2021JD034888

Li, S., Park, S., Lee, J.-Y., Ha, K.-J., Park, M.-K., Jo, C. O., Oh, H., Mühle, J., Kim, K.-R., Montzka, S. A., O'Doherty, S., Krummel, P. B., Atlas, E., Miller, B. R., Moore, F., Weiss, R. F., & Wofsy, S. C. (2018). Chemical evidence of inter-hemispheric air mass intrusion into the Northern Hemisphere mid-latitudes. *Scientific Reports*, *8*(1), 4669. https://doi.org/10.1038/s41598-018-22266-0

Marks, J., & Bayliss, C. (2011). IAI 2010 anode effect survey results. *Aluminium International Today*, *23*(5), 15–16, 18. Retrieved February 4, 2024, from https://www.proquest.com/docview/1009072373/abstract/3ECB7B2FFDA6449CPQ/1

Marks, J., & Nunez, P. (2018). Updated Factors for Calculating PFC Emissions from Primary Aluminum Production. In O. Martin (Ed.), *Light Metals 2018* (pp. 1519–1525). Springer International Publishing. https://doi.org/10.1007/978-3-319-72284-9_198

Miller, B. R., Weiss, R. F., Salameh, P. K., Tanhua, T., Greally, B. R., Mühle, J., & Simmonds, P. G. (2008). Medusa: A Sample Preconcentration and GC/MS Detector System for in Situ Measurements of Atmospheric Trace Halocarbons, Hydrocarbons, and Sulfur Compounds. *Analytical Chemistry*, *80*(5), 1536–1545. https://doi.org/10.1021/ac702084k

Ministry of Ecology and Environment. (2018, December). *The People's Republic of China Second Biennial Update Report on Climate Change* (tech. rep.). https://unfccc.int/documents/636696

Ministry of Ecology and Environment. (2024, December). *The People's Republic of China First Biennial Transparency Report on Climate Change* (tech. rep.). Retrieved January 8, 2025, from https://unfccc.int/sites/default/files/resource/The%20People%E2%80%99s%20Republic%20of%20China%20First%20Biennial%20Transparency%20Report%20on%20Climate%20Change.pdf

MoEFCC. (2024, December). *India Fourth Biennial Update Report* (tech. rep.). New Delhi. Retrieved February 15, 2025, from https://unfccc.int/sites/default/files/resource/India%20BUR-4.pdf

Morris, R. A., Miller, T. M., Viggiano, A. A., Paulson, J. F., Solomon, S., & Reid, G. (1995). Effects of electron and ion reactions on atmospheric lifetimes of fully fluorinated compounds. *Journal of Geophysical Research: Atmospheres*, *100*(D1), 1287–1294. https://doi.org/10.1029/94JD02399

Mühle, J., Ganesan, A. L., Miller, B. R., Salameh, P. K., Harth, C. M., Greally, B. R., Rigby, M., Porter, L. W., Steele, L. P., Trudinger, C. M., Krummel, P. B., O'Doherty, S.,

Fraser, P. J., Simmonds, P. G., Prinn, R. G., & Weiss, R. F. (2010). Perfluorocarbons in the global atmosphere: Tetrafluoromethane, hexafluoroethane, and octafluoropropane. *Atmospheric Chemistry and Physics*, *10*(11), 5145–5164. https://doi.org/10.5194/acp-10-5145-2010

Nishida, H., Matsumura, K., Kurokawa, H., Hoshino, A., & Masui, S. (2005). PFC emission-reduction strategy for the LCD industry. *Journal of the Society for Information Display*, *13*(10), 841–848. https://doi.org/10.1889/1.2121068

Olivier, J. G. J. (2022). *Trends in global CO2 and total greenhouse gas emissions: 2021 Summary report* (tech. rep.). PBL Netherlands Environmental Assessment Agency. The Hague.

Ou, S., Yang, Q., & Liu, J. (2024). The global production pattern of the semiconductor industry: An empirical research based on trade network. *Humanities and Social Sciences Communications*, *11*(1), 750. https://doi.org/10.1057/s41599-024-03253-5

Pawlek, R. P. (2023, November). Primary Aluminum Producers. Retrieved March 5, 2025, from https://www.lightmetalage.com/resources-section/primary-producers/

Penkett, S. A., Prosser, N. J. D., Rasmussen, R. A., & Khalil, M. a. K. (1981). Atmospheric measurements of CF4 and other fluorocarbons containing the CF3 grouping. *Journal of Geophysical Research: Oceans*, *86*(C6), 5172–5178. https://doi.org/10.1029/JC086iC06p05172

Pisso, I., Sollum, E., Grythe, H., Kristiansen, N. I., Cassiani, M., Eckhardt, S., Arnold, D., Morton, D., Thompson, R. L., Groot Zwaaftink, C. D., Evangeliou, N., Sodemann, H., Haimberger, L., Henne, S., Brunner, D., Burkhart, J. F., Fouilloux, A., Brioude, J., Philipp, A., … Stohl, A. (2019). The Lagrangian particle dispersion model FLEXPART version 10.4. *Geoscientific Model Development*, *12*(12), 4955–4997. https://doi.org/10.5194/gmd-12-4955-2019

Platt, S. M., Svendby, T. M., Hermansen, O., Lunder, C. R., Fiebig, M., Fjæraa, A. M., Duflot, V., Schmidbauer, N., Myhre, C. L., Yttri, K. E., Eckhardt, S., & Stebel, K. (2024). *Monitoring of greenhouse gases and aerosols at Svalbard and Birkenes in 2023. Annual report* (tech. rep.). NILU. Retrieved January 27, 2025, from https://nilu.brage.unit.no/nilu-xmlui/handle/11250/3171271

Prinn, R. G., Weiss, R. F., Arduini, J., Arnold, T., DeWitt, H. L., Fraser, P. J., Ganesan, A. L., Gasore, J., Harth, C. M., Hermansen, O., Kim, J., Krummel, P. B., Li, S., Loh, Z. M., Lunder, C. R., Maione, M., Manning, A. J., Miller, B. R., Mitrevski, B., … Zhou, L. (2018). History of chemically and radiatively important atmospheric gases from the Advanced Global Atmospheric Gases Experiment (AGAGE). *Earth System Science Data*, *10*(2), 985–1018. https://doi.org/10.5194/essd-10-985-2018

Ravishankara, A. R., Solomon, S., Turnipseed, A. A., & Warren, R. F. (1993). Atmospheric Lifetimes of Long-Lived Halogenated Species. *Science*, *259*(5092), 194–199. https://doi.org/10.1126/science.259.5092.194

Rigby, M., Prinn, R. G., O'Doherty, S., Miller, B. R., Ivy, D., Mühle, J., Harth, C. M., Salameh, P. K., Arnold, T., Weiss, R. F., Krummel, P. B., Steele, L. P., Fraser, P. J., Young, D., & Simmonds, P. G. (2014). Recent and future trends in synthetic greenhouse gas radiative forcing. *Geophysical Research Letters*, *41*(7), 2623–2630. https://doi.org/10.1002/2013GL059099

Roehl, C. M., Boglu, D., Brühl, C., & Moortgat, G. K. (1995). Infrared band intensities and global warming potentials of CF4, C2F6, C3F8, C4F10, C5F12, and C6F14. *Geophysical Research Letters*, *22*(7), 815–818. https://doi.org/10.1029/95GL00488

Say, D., Manning, A. J., Western, L. M., Young, D., Wisher, A., Rigby, M., Reimann, S., Vollmer, M. K., Maione, M., Arduini, J., Krummel, P. B., Mühle, J., Harth, C. M., Evans, B., Weiss, R. F., Prinn, R. G., & O'Doherty, S. (2021). Global trends and European emissions of tetrafluoromethane (CF_4), hexafluoroethane (C_2F_6) and octafluoropropane (C_3F_8). *Atmospheric Chemistry and Physics*, *21*(3), 2149–2164. https://doi.org/10.5194/acp-21-2149-2021

Seibert, P., & Frank, A. (2004). Source-receptor matrix calculation with a Lagrangian particle dispersion model in backward mode. *Atmospheric Chemistry and Physics*, *4*(1), 51–63. https://doi.org/10.5194/acp-4-51-2004

Sharma, D., & Mauzerall, D. (2021). Analysis of Air Pollution Data in India between 2015 and 2019. *Aerosol and Air Quality Research*, *22*(2), 210204. https://doi.org/10.4209/aaqr.210204

Stohl, A., Hittenberger, M., & Wotawa, G. (1998). Validation of the lagrangian particle dispersion model FLEXPART against large-scale tracer experiment data. *Atmospheric Environment*, *32*(24), 4245–4264. https://doi.org/10.1016/S1352-2310(98)00184-8

Tabereaux, A. T., & Peterson, R. D. (2014, January). Chapter 2.5 - Aluminum Production. In S. Seetharaman (Ed.), *Treatise on Process Metallurgy* (pp. 839–917). Elsevier. https://doi.org/10.1016/B978-0-08-096988-6.00023-7

Tan, C., Yu, X., Li, D., Lei, T., Hao, Q., & Guan, D. (2025). Different technology packages for aluminium smelters worldwide to deliver the 1.5 °C target. *Nature Climate Change*, *15*(1), 51–58. https://doi.org/10.1038/s41558-024-02193-x

Tarantola, A. (2005, January). *Inverse Problem Theory and Methods for Model Parameter Estimation*. Society for Industrial; Applied Mathematics. Retrieved November 14, 2023, from http://epubs.siam.org/doi/book/10.1137/1.9780898717921

Thacker, W. C. (2007). Data assimilation with inequality constraints. *Ocean Modelling*, *16*(3), 264–276. https://doi.org/10.1016/j.ocemod.2006.11.001

Thompson, R. L., & Stohl, A. (2014). FLEXINVERT: An atmospheric Bayesian inversion framework for determining surface fluxes of trace species using an optimized grid. *Geoscientific Model Development*, *7*(5), 2223–2242. https://doi.org/10.5194/gmd-7-2223-2014

Trudinger, C. M., Fraser, P. J., Etheridge, D. M., Sturges, W. T., Vollmer, M. K., Rigby, M., Martinerie, P., Mühle, J., Worton, D. R., Krummel, P. B., Steele, L. P., Miller, B. R., Laube, J., Mani, F. S., Rayner, P. J., Harth, C. M., Witrant, E., Blunier, T., Schwander, J., ... Battle, M. (2016). Atmospheric abundance and global emissions of perfluorocarbons CF_4, C_2F_6 and C_3F_8 since 1800 inferred from ice core, firn, air archive and in situ measurements. *Atmospheric Chemistry and Physics*, *16*(18), 11733–11754. https://doi.org/10.5194/acp-16-11733-2016

UNFCCC. (1997, October). *Kyoto Protocol to the United Nations Framework Convention on Climate Change* (tech. rep.). Kyoto. Retrieved November 18, 2024, from https://unfccc.int/kyoto_protocol

UNFCCC. (2012, March). *Report of the Conference of the Parties on its seventeenth session* (tech. rep.). Durban. Retrieved November 18, 2024, from https://unfccc.int/biennial-update-reports

UNFCCC. (2024a). Greenhouse Gas Inventory Data - Flexible queries Annex I countries. Retrieved November 12, 2024, from https://di.unfccc.int/flex_annex1

UNFCCC. (2024b). Greenhouse Gas Inventory Data - Flexible queries Non Annex I countries. Retrieved November 12, 2024, from https://di.unfccc.int/flex_non_annex1

Vimont, I., Montzka, S., & Elkins, J. (2015). NOAA Global Monitoring Laboratory. Retrieved January 27, 2025, from https://gml.noaa.gov

Vogel, H., & Friedrich, B. (2018). An Estimation of PFC Emission by Rare Earth Electrolysis. In O. Martin (Ed.), *Light Metals 2018* (pp. 1507–1517). Springer International Publishing. https://doi.org/10.1007/978-3-319-72284-9_197

Vojta, M., Plach, A., Annadate, S., Park, S., Lee, G., Purohit, P., Lindl, F., Lan, X., Mühle, J., Thompson, R. L., & Stohl, A. (2024). A global re-analysis of regionally resolved emissions and atmospheric mole fractions of SF_6 for the period 2005–2021. *Atmospheric Chemistry and Physics*, *24*(21), 12465–12493. https://doi.org/10.5194/acp-24-12465-2024

Vojta, M., Plach, A., Thompson, R. L., Purohit, P., Stanley, K., O'Doherty, S., Young, D., Pitt, J., Lan, X., & Stohl, A. (2025). A thousand inversions to determine European SF_6 emissions from 2005 to 2021. *EGUsphere*, 1–64. https://doi.org/10.5194/egusphere-2025-1095

Vojta, M., Plach, A., Thompson, R. L., & Stohl, A. (2022). A comprehensive evaluation of the use of Lagrangian particle dispersion models for inverse modeling of greenhouse gas

emissions. *Geoscientific Model Development*, *15*(22), 8295–8323. https://doi.org/10.5194/gmd-15-8295-2022

Wong, D. S., Fraser, P., Lavoie, P., & Kim, J. (2015). PFC Emissions from Detected Versus Nondetected Anode Effects in the Aluminum Industry. *JOM*, *67*(2), 342–353. https://doi.org/10.1007/s11837-014-1265-8

WSC. (2011, May). *Joint Statement of the 15th Meeting of the World Semiconductor Council (WSC)* (tech. rep.). Fukuoka, Japan. Retrieved November 17, 2024, from http://www.semiconductorcouncil.org/wp-content/uploads/2016/07/WSC_2011_Joint_Statement.pdf

WSC. (2021, February). *Joint Statement of the 25th Meeting of the World Semiconductor Council (WSC)* (tech. rep.). Virtual. Retrieved November 17, 2024, from http://www.semiconductorcouncil.org/wp-content/uploads/2021/08/FINAL-25th-WSC-Joint-Statement_0602.pdf

WSC. (2024, June). *Joint Statement of the 28th Meeting of the World Semiconductor Council (WSC)* (tech. rep.). Miyazaki, Japan. Retrieved November 16, 2024, from http://www.semiconductorcouncil.org/wp-content/uploads/2024/06/2024-WSC-Joint-Statement-FINAL.pdf

Yao, B., Vollmer, M. K., Zhou, L. X., Henne, S., Reimann, S., Li, P. C., Wenger, A., & Hill, M. (2012). In-situ measurements of atmospheric hydrofluorocarbons (HFCs) and perfluorocarbons (PFCs) at the Shangdianzi regional background station, China. *Atmospheric Chemistry and Physics*, *12*(21), 10181–10193. https://doi.org/10.5194/acp-12-10181-2012

Acronyms

AE anode effects.

AGAGE Advanced Global Atmospheric Gases Experiment.

BU bottom-up.

C_2F_6 hexafluoroethane.

C_3F_8 octafluoropropane.

CF_4 tetrafluoromethane.

CH_4 methane.

CMA Chinese Meteorological Administration.

CO_2 carbon dioxide.

CTM Chemical Transport Model.

CVD chemical vapor deposition.

ECMWF European Centre for Medium-Range Weather Forecasts.

EDGAR Emissions Database for Global Atmospheric Research.

GDB global-distribution-based.

GFC global financial crisis.

GHG greenhouse gas.

GWP global warming potential.

IAI International Aluminium Institute.

IPCC Intergovernmental Panel on Climate Change.

ITCZ Inter-Tropical Convergence Zone.

LCM Linear Chemistry Module.

LOGOS Long-term Observations of Greenhouse gases and Ozone-depleting Substances.

LPDM Lagrangian Particle Dispersion Model.

NF_3 nitrogen trifluoride.

NH Northern Hemisphere.

NILU Norwegian Institute for Air Research.

NOAA-ESRL-GML National Oceanic and Atmospheric Administration, Earth System Research Laboratories, Global Monitoring Laboratory.

PFC perfluorocarbon.

SF_6 sulfur hexafluoride.

SH Southern Hemisphere.

SRR source receptor relationship.

TD top-down.

UNFCCC United Nations Framework Convention on Climate Change.

A. Appendix I

ID	Station name	Organisation	Location	Altitude	Interval	Period
AKD	Akedala, China	CMA	47.1°N, 87.6°E	562m	1w	08.2017-10.2021
ALT	Alert, Canada	NOAA-ESRL-GML	82.5°N, 62.5°W	185m	1w-1m	10.2014-05.2021
AMY	Anmyeon-do, South Korea	NOAA-ESRL-GML	36.5°N, 126.3°E	47m	3m	12.2018-07.2021
BRW	Barrow, USA	NOAA-ESRL-GML	71.3°N, 156.6°W	11m	2w	10.2014-07.2021
HFM	Harvard Forest, USA	NOAA-ESRL-GML	42.5°N, 72.2°W	340m	2w	11.2014-05.2021
JGJ	Jiangjin, China	CMA	29.2°N, 106.2°E	262m	1d	03.2017-12.2021
JSA	Jinsha, China	CMA	29.6°N, 114.2°E	750m	1w	01.2019-11.2021
KUM	Cape Kumukahi, USA	NOAA-ESRL-GML	19.6°N, 154.9°W	8m	2w	09.2014-08.2021
LAN	Lin'an, China	CMA	30.3°N, 119.7°E	138m	1d	01.2011-11.2021
LEF	Park Falls, USA	NOAA-ESRL-GML	45.9°N, 90.3°W	472m	2w	10.2014-10.2020
LFS	Longfengshan, China	CMA	44.7°N, 127.6°E	330m	1w	01.2011-10.2021
MLO	Mauna Loa, USA	NOAA-ESRL-GML	19.5°N, 155.6°W	3397m	2w	09.2014-11.2021
NWR	Niwot Ridge, USA	NOAA-ESRL-GML	40.1°N, 105.6°W	3523m	1m	11.2014-11.2021
PSA	Palmer Station, Antarctica	NOAA-ESRL-GML	64.8°S, 64.1°W	10m	1m	07.2014-06.2021
SPO	South Pole, Antarctica	NOAA-ESRL-GML	90.0°S, 24.8°W	2810m	1m	02.2014-10.2021
SUM	Summit, Greenland	NOAA-ESRL-GML	82.6°N, 38.4°W	3210m	1m	08.2014-07.2021
TRL	Trollhaugen, Antarctica	NILU	72.0°S, 2.5°W	1558m	1m	03.2008-06.2024

(continued on next page)

ID	Station name	Organisation	Location	Altitude	Interval	Period
WLG	Mt. Waliguan, China	CMA	36.3°N, 100.9°E	3816m	1w	01.2011-11.2021
XFG	Xinfeng, China	CMA	24.1°N, 114.2°E	870m	1w	08.2018-11.2021
XGL	Shangri-La, China	CMA	28.0°N, 99.4°E	3580m	1w	07.2011-10.2021

Tab. A1 Sites of atmospheric flask measurements. Note: Altitude is given in m.a.s.l.